Supported Erythrocyte Membranes on Piezoelectric Sensors for Studying the Interactions with Nanoparticles

October 25, 2023

Tanaz Islam,[†] Olga N. Chesnokov,[‡] Andrew V. Oleinikov,[‡] and 易鹏 (Yi, Peng)[†, *]

[†]*Department of Civil, Environmental and Geomatics Engineering, College of Engineering & Computer Science, Florida Atlantic University, Boca Raton, Florida 33431-6496*

[‡]*Department of Biomedical Science, Charles E. Schmidt College of Medicine, Florida Atlantic University, Boca Raton, Florida 33431-6496*

* Corresponding author: Peng Yi, Email: pengyi0124@outlook.com

ABSTRACT

Applications of nanoparticles (NPs) in nanodrugs, food additives, and cosmetics can result in the presence of nanomaterials in human circulatory system and their attachment to red blood cells (RBCs), which may lead to cytotoxic effects. To investigate the interactions of NPs with RBC membranes (RBCm), supported erythrocyte membranes (SRBCm) were developed on the piezoelectric sensors in a quartz crystal microbalance with dissipation (QCM-D) at 25 °C. A well dispersed RBCm suspension at 1 mM NaCl and 0.2 mM $NaHCO_3$ was obtained from whole blood, and comprised of colloidal membrane fragments with the average hydrodynamic diameter and zeta potential as 390 nm and -0.53 mV, respectively, at pH 7.0. The thin and rigid SRBCm was formed mainly through the deposition of RBCm fragments on the poly-L-lysine modified crystal sensor, leading to the average frequency shift of -26.2 Hz and the low ratio of dissipation to frequency shift (7.2×10^{-8} Hz^{-1}). The complete coverage of SRBCm was indicated by the plateau of frequency shift in the stage of SRBCm formation and no deposition of negatively charged 106 nm polystyrene nanoparticles (PSNPs) on the SRBCm. Atomic force microscopy and immunofluorescence microscopy images showed that RBCm aggregates with the average size of 420 nm and erythrocyte membrane proteins existed on SRBCm, respectively. The methods of determining attachment efficiencies of model positively charged NPs (i.e., hematite NPs or HemNPs) and model negatively charged NPs (i.e., PSNPs) on SRBCm were demonstrated in 1 mM NaCl solution at pH 5.1 and pH 7.0, respectively. HemNPs exhibited a favorable deposition with an attachment efficiency of 0.99 while PSNPs did not show any attachment propensity toward SRBCm.

KEYWORDS: Supported red blood cell membrane, phospholipid bilayers, QCM-D, cryo-TEM, immunofluorescence microscopy

INTRODUCTION

In recent years, nanoparticles (NPs) have been increasingly used in pharmaceutical and biotechnology industries for diagnosis, imaging, and targeted drug delivery. Orally administered Gastromark™ (silicone-coated superparamagnetic iron oxide NPs) has been used as contrast agents in gastrointestinal magnetic resonance imaging (MRI).[1] Ferumoxytol also known as

Feraheme™ (carbohydrate-coated Fe_3O_4 NPs) has been approved by U.S. Food and Drug Administration (FDA) to treat iron deficiency anemia for adult patients through intravenous administration.[2, 3] Liposomal nanodrugs like Doxil® and Onivyde® are injected for targeted drug delivery for cancer patients.[2, 4] Administration of such drugs leads to direct contact of blood cells with the NPs.[2] In addition, NPs, such as TiO_2 NPs,[5, 6] have been extensively added in food additives,[6, 7] food packaging,[8] and cosmetics,[5, 8] likely resulting in the entry of NPs into human digestive systems via different routes.[9, 10] Following the entry into the gastrointestinal system, NPs could penetrate through epithelial and endothelial barriers into the bloodstream and lymph stream.[11, 12] Also, carbon black NPs that are released into the air from combustion engines and power plants can enter human respiratory systems, translocate from the lung to the circulation system,[13-17] and easily be distributed to lymph nodes, liver, heart, kidney, and brain.[18-21] Using gold NPs as model NPs, Miller et al.[13, 22] detected ~35 ng/L gold in the urine of human subjects after 2-hour inhalation of the air containing 116 $\mu g/m^3$ 5 nm gold NPs.

The NPs in the digestive, respiratory, and circulatory system will inevitably contact with and attach to human cells[11, 23-25] such as epithelial, endothelial, and blood cells (i.e., red blood cells, white blood cells, and platelets). Such attachment of nanoparticles to cell membranes has been proposed to be crucial for NPs to exert cytotoxic effects,[26-28] since it is a critical step toward the disruption of cell membrane and cellular processes.[30] The attachment of hematite NPs (HemNPs) to human epithelial cell lines was shown to be a very important step for the uptake of HemNPs by the cells, which resulted in the loss of membrane integrity and the release of cytokines, e.g., interleukin-6 that is known to promote inflammatory responses.[29] It was also reported that the contact of HemNPs with myoblast cancer cells formed small pores in the membrane through which NPs entered inside and damaged organelles, triggering cell death and apoptosis of cells.[30] In addition, the attachment of polystyrene NPs (PSNPs), commonly used as model plastic NPs,[31] to human intestinal epithelial cells resulted in cellular internalization of PSNPs and partial colocalization of PSNPs in lysosome,[32] raising concerns on the chronic effects of ingested plastic NPs. In order to estimate the cytotoxic effects of NPs on human cells, it is crucial to first measure the probability of NPs attaching to the membranes of human cells upon contact.

In particular, erythrocytes or red blood cells (RBCs), a dominant type of blood cells having the highest chance to encounter the NPs present in the blood stream, is vulnerable to toxicity like deformation, agglutination and membrane damage when they come to contact with the NPs.[19] For

example, attachment of PSNPs to RBCs was found to increase the osmotic, mechanical and oxidative stress which resulted in sensitization and cell damage of RBCs.[33] In addition, several methodologies have been proposed to utilize RBCs as drug carriers for the targeted delivery of nanodrugs in the human body,[34, 35] due to the bioavailability, biocompatibility, and longevity of RBCs in the circulation system.[33, 36] Brenner et al.,[35] used the surface of RBCs as a hitchhiking tool on which nanocarriers (e.g., nanogel, liposomes, etc.) were adsorbed and transported to the first organ downstream of the intravascular injection. In another study, doxorubicin-loaded poly(lactic-co-glycolic acid) (PLGA) NPs were hitchhiked onto the surface of RBCs for targeted delivery of this chemotherapy drug for lung metastasis treatment.[34] Thus, from both perspectives of nanoparticle toxicity and nanodrug delivery, it is important to quantitatively study the attachment of NPs to the membranes of RBCs.

Some prior research works studied the attachment of different NPs to the surface of whole RBCs using various observational tools such as scanning electron microscopy (SEM), conventional optical microscopy, transmission electron microscopy (TEM), and confocal laser scanning microscopy (CLSM). For instance, TEM was used to locate TiO_2-NP (~20 nm) aggregates attached to the membrane of RBCs.[19] The attachment of PSNPs (200 nm) to RBCs was observed using SEM after incubation at the particle/RBC ratio up to 100:1.[33, 37, 38] Nevertheless, quantitative information on the probability of NPs' attachment to the membranes of human RBCs is still rare due to the lack of appropriate tools.

Recently, piezoelectric sensors, e.g., quartz crystal microbalance (QCM) sensors coated with supported lipid bilayer (SLBs) of synthetic phospholipids such as palmitoyl-2-oleoyl-*sn*-glycero-3-phosphocholine (POPC), 1, 2-dioleoyl-*sn*-glycero-3-phosphocholine (DOPC), etc. have been employed to conduct quantitative studies on interactions between NPs and model cell membranes.[39-42] For example, Yi and Chen[39] used DOPC SLBs on silica-coated QCM crystals for studying the deposition attachment efficiency (i.e., the probability of attachment upon contact) of carboxylated multiwalled carbon nanotubes on model cell membranes. The advancement has been seen in the field of SLBs by incorporating sterols,[43] charged lipids such as phosphatidylinositol,[44] phosphatidylserine,[45] and phosphatidylglycerol,[46] and cell penetrating peptides[46] in SLBs. Moreover, Melby et al.[47] formed a lipid raft system incorporating highly ordered domains of sphingomyelin and cholesterol in a DOPC SLB. However, such SLBs still cannot fully replicate the complex characteristics of real cell membrane of a mammalian cell.

Some early efforts have been made in fixing real cell membranes on the surface of substrates. Himbert et al.[48] deposited RBC membrane (RBCm) vesicles prepared via hypotonic treatment and sonication on hydrophilic silicon wafers. The RBCm seemed to form a smooth layer under an optical microscope after a slow drying process at 50 °C and a relative humidity of 95.8 ± 0.5% for 5 days. In another study,[49] the suspension of RBCm also prepared through hypotonic hemolysis and sonication, was dispensed on the Au screen printed electrode coated with enzyme composites. The RBCm layer with the electrode was dried in an oven at 50 °C for 50 min. The SEM and atomic force microscopy (AFM) images revealed that there were many bumps in the size of 0.1–3 μm on the surface of the dry RBCm layer. In both studies, the drying processes at 50 °C may have increased the membrane fluidity and led to an irreversible change in membrane elasticity,[50] protein denaturation[51] and enzyme inactivation.[52] Thus, the original biological features of RBCm may have been lost in those layers. Tanaka et al.[53] deposited RBC ghosts (i.e., empty cells with only RBC membranes) on a poly-L-lysine (PLL) coated glass slide through 60 min incubation and the following rinsing both in a 0.5 mM phosphate buffer at room temperature. As a result, the surface of glass slide was partially covered by the patches of RBC ghosts. As for other cells, Ehrenhöfer et al.[54] developed the technique to peel the membrane from kidney cells using the mica surface coated with positively charged iberiotoxin for subsequent AFM imaging in a physiological solution. Similarly, Perez et al.[55] peeled ~30 × 30 μm^2 membranes from swelled HEK-293 cells using PLL-coated glass coverslips which also served as the substrates during microscopic observations. The membranes peeled from various cells so far had areas of 100-1000 μm^2 which is too small to be applied on conventional sensors.[56] To the best of our knowledge, no piezoelectric sensor has been completely coated with real cell membranes for quantifying the attachment probability of NPs.

In this study, supported RBCm (SRBCm) has been developed on piezoelectric sensors (i.e., QCM crystals) in aqueous solution at room temperature. The surface morphology of SRBCm has been characterized using AFM and the distribution of surface proteins of RBCs on SRBCm was characterized using immunofluorescence microscopy (IFM). The attachment efficiencies of the negatively charged nanoparticles (e.g., PSNPs) and positively charged nanoparticles (e.g., HemNPs) on SRBCm were quantified using QCM for demonstration purpose. Two different deposition behaviors of HemNPs were observed on SRBCm depending on the aggregation propensity of HemNPs.

RESULTS AND DISCUSSION

Preparation and Characterization of RBC Membrane Suspension. In order to develop a SRBCm on the QCM sensor, RBCm suspension was first prepared. Erythrocytes were isolated from plasma and buffy coat after centrifugation of the whole blood, and then washed 3 times by phosphate-buffered saline (PBS) followed by the hypotonic treatment in 4-time diluted PBS and the resultant hemolysis. The remaining RBCm ghosts were sequentially washed by 4-time diluted PBS and deionized (DI) water before they were stored in DI water under static condition at 3°C in a refrigerator for 3 days. After that, the RBCm ghosts were fully dispersed into colloidal fragments. Right before use, probe sonication was applied to further reduce the size of RBCm fragments and the solution chemistry of the suspension was adjusted to be 1 mM NaCl and 0.2 mM $NaHCO_3$. The final concentration of RBCm in the working suspensions was equal to 60% of the RBCm concentration in the original whole blood. More detailed information is available in the section of Materials and Methods.

The photograph of dispersed RBC membranes in a solution of 1 mM NaCl and 0.2 mM $NaHCO_3$ (pH 7.0) after sonication is shown in Figure 1a, which looks like a translucent colloidal suspension. The cryogenic transmission electron microscopy (cryo-TEM) images of RBCm suspension are presented in Figure 1b, 1c, and 1d, which reveal that erythrocyte membrane had been broken off into colloidal fragments in the suspension. Some small fragments were amorphous in size or shape, as pointed out by the yellow arrows in Figure 1b. Some fragments were attached to each another developing RBCm aggregates indicated by the red oval in Figure 1b. Its size was approximately 450 nm in short diameter and 700 nm in long diameter. A thin and large piece of RBCm fragment was observed in Figure 1c, with a length of 1200 nm and a width of 900 nm. Moreover, a vesicle-like structure with the RBCm thickness of 5 nm was observed in Figure 1d as pointed out by the green arrow. The intensity-weighted hydrodynamic diameter of the RBCm colloidal fragments including RBCm aggregates and vesicles in the suspension was determined by dynamic light scattering (DLS) as 390 ± 90 nm (avg. ± std. dev.). The zeta potential of RBCm fragments was determined as -0.53 ± 0.41 mV (avg. ± std. dev.) in the solution of 1 mM NaCl and 0.2 mM $NaHCO_3$ at pH 7.0.

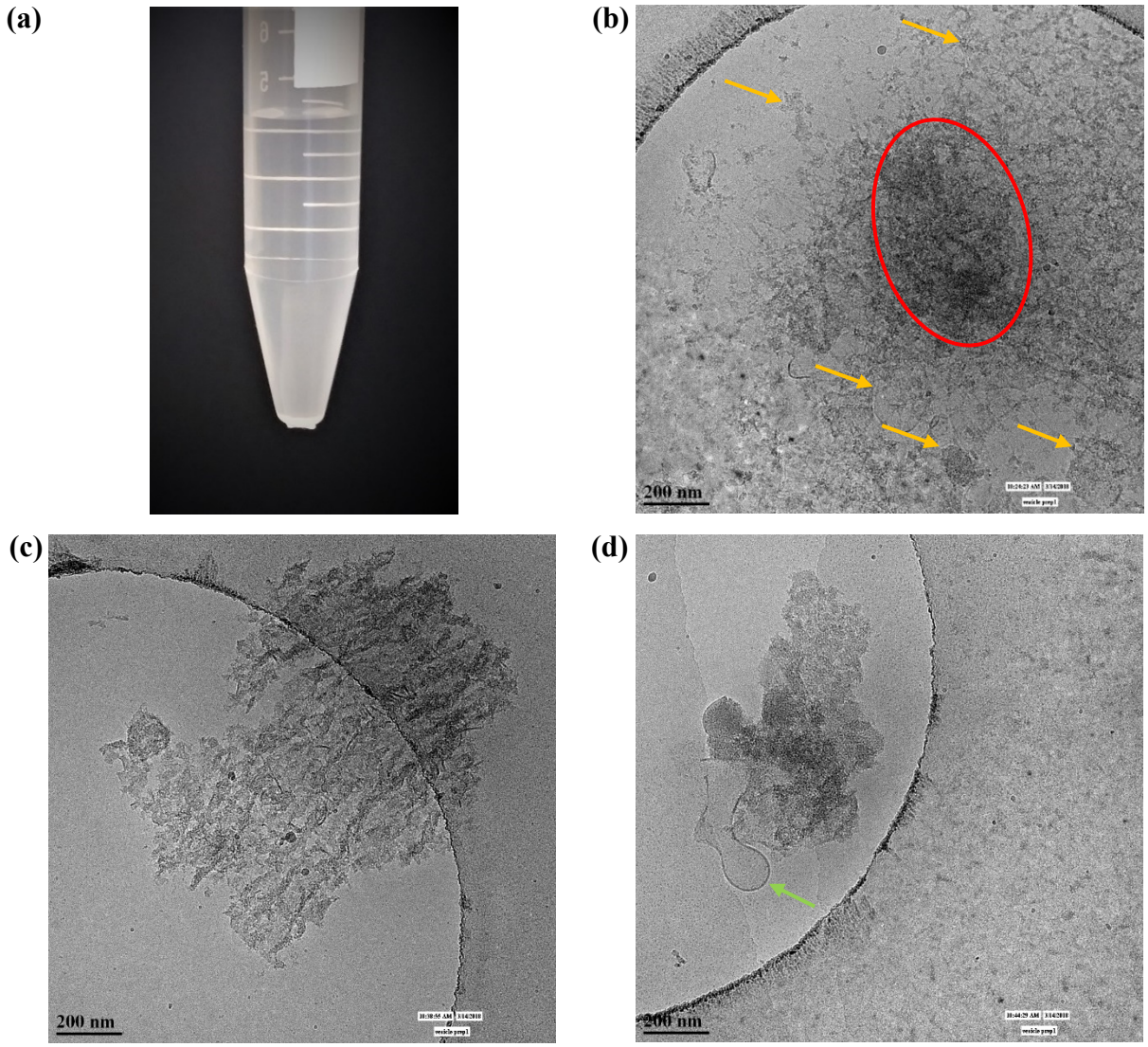

Figure 1. (a) A photograph of RBCm colloidal suspension (at 60% of the original RBCm concentration in the whole blood) in a solution of 1 mM NaCl and 0.2 mM $NaHCO_3$ (pH 7.0). The suspension was used for the formation of supported erythrocyte membrane. Cryo-TEM images of RBCm fragments dispersed in a solution of 1 mM NaCl and 0.2 mM $NaHCO_3$: (b) Small RBCm fragments indicated by yellow arrows and the RBCm aggregate outlined by the red oval, (c) a large piece of RBCm fragment, and (d) a vesicle-like structure with the RBCm thickness of 5 nm indicated by the green arrow.

Formation of Supported RBCm on a Silica-Coated Piezoelectric Sensor. The supported RBCm (SRBCm) layer was developed on a silica-coated piezoelectric sensor of a quartz crystal microbalance with dissipation monitoring (QCM-D). Figure 2 presents the representative

normalized frequency and dissipation shifts at the third overtone, denoted as $\Delta f_{(3)}$ (i.e., $\Delta f_3/3$)[57, 58] and $\Delta D_{(3)}$, respectively, of the sensor during the formation of the SRBCm. A stable baseline was first obtained by rinsing the substrate surface with deionized (DI) water at 0.1 mL/min. Then, according to a well-established procedure,[58, 59] the negatively charged sensor surface was completely coated by a cationic layer of PLL by sequentially introducing ~2 mL of HEPES buffer [i.e., 10 mM *N*-(2-hydroxyethyl) piperazine-*N'*-(2-ethanesulfonic acid) (HEPES) and 100 mM NaCl], ~2 mL of 0.1 g/L PLL dissolved in HEPES buffer, and ~2 mL of HEPES buffer across the sensor surface. After obtaining stable baselines of frequency and dissipation by rinsing the PLL-modified surface with a background electrolyte solution of 1 mM NaCl and 0.2 mM $NaHCO_3$ at pH 7.0, the RBCm suspension at the same solution chemistry was introduced into the measurement chamber.

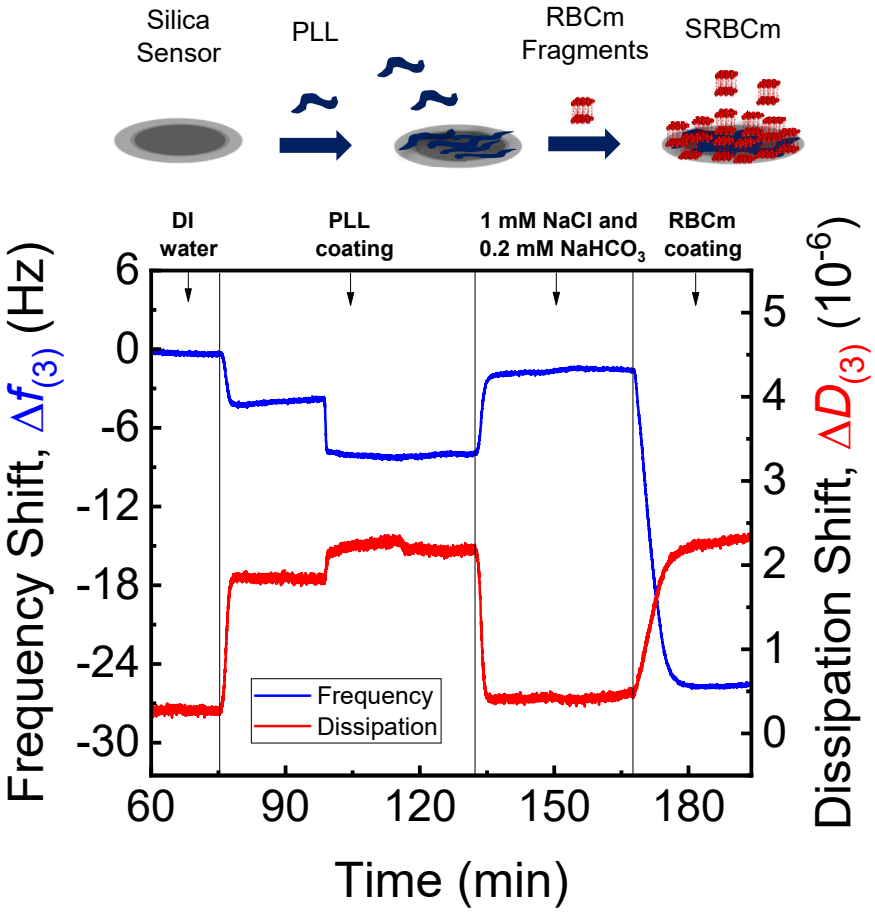

Figure 2. Formation of supported erythrocyte membrane on a silica-coated piezoelectric sensor. Representative frequency and dissipation responses were obtained by the QCM-D during the

formation process of supported erythrocyte membrane on PLL-modified silica sensor at 1 mM NaCl and 0.2 mM $NaHCO_3$, pH 7.0.

As shown in Figure 2, $\Delta f_{(3)}$ decreased and $\Delta D_{(3)}$ increased sharply due to the deposition of RBCm fragments on PLL-modified sensor surface. As the colloidal fragments of RBC membrane and PLL layer carried negative and positive surface charge,[39, 58] respectively, at pH 7.0, the deposition of RBCm fragments on the PLL-modified surface was favorable due to electrostatic attraction. Both frequency and dissipation attained plateaus in 13 min after the starting of deposition, signifying that, the surface of sensor had been completely coated with RBCm fragments and no multilayer deposition took place. The overall $\Delta f_{(3)}$ and $\Delta D_{(3)}$ of RBCm coating was determined as -26.2 ± 4.1 Hz (avg. ± std. dev.), and 1.87 ± 0.48 × 10^{-6} (avg. ± std. dev.), respectively, based on ten experiments. The low $\left|\Delta D_{(3)}/\Delta f_{(3)}\right|$ of 7.2 ± 1.5×10^{-8} Hz^{-1} (avg. ± std. dev.) indicates that the deposited RBCm fragments formed a thin and rigid layer.[60] Previous QCM-D studies showed that the formation of SLBs comprised of just phospholipids led to Δf of -25 ± 3 Hz and ΔD of < 0.2 × 10^{-6}.[39, 60-63] When SLBs incorporated other types of biomacromolecules such as sterols, peptides, phosphatidylglycerol, etc., the normalized frequency shifts and dissipation shifts resulted from SLB formation were -26 – -28 Hz and 0.51–1.5 × 10^{-6}, respectively.[44, 46, 47] The similarity of frequency and dissipation shifts of deposited layer of RBCm to that of SLBs, suggests that the supported RBCm layer had similar thickness and structure as SLBs. The thickness of egg phosphatidyl choline SLBs was estimated as ~4 nm from the $\Delta f_{(3)} \approx$ -26 Hz and $\Delta D_{(3)} \approx 0$ using Sauerbrey equation and a density of 1.1 g/cm^3.[64] Thus, we speculate that the SRBCm was mainly a single layer of flattened fragments of RBCm which completely covered the surface of PLL-modified sensor, as illustrated by the cartoon in Figure 2, through primarily the deposition of RBCm fragments and possibly the spreading of RBCm upon the attachment of RBCm vesicles to the PLL layer. Since RBCm fragments were pieces of original erythrocyte membranes, the SRBCm should retain important biological components of cell membrane, i.e., phospholipid bilayer, sterols, proteins, etc.

Completeness of Supported RBCm Coating. As mentioned in the previous section, the plateaus of $\Delta f_{(3)}$ and $\Delta D_{(3)}$ that formed within the first 6-13 mins of SRBCm formation stages (Figure 2 and Figure S3-S5, in Supporting Information) indicate the complete coverage of SRBCm on the

underlying PLL layer and no multilayer deposition of RBCm. Otherwise, a continued decrease of frequency should have been observed. For the study of deposition of NPs on SRBCm, the complete coverage of SRBCm was further tested through deposition experiments of carboxylated polystyrene nanoparticles (PSNPs) on SRBCm. The hydrodynamic diameter of PSNPs was determined to be 106 ± 3 nm (avg. ± std. dev.) from the DLS measurements. As shown in Figure 3a, a supported erythrocyte membrane was developed first using the same procedure as described earlier. Following the stable baseline in the background solution (i.e., 1 mM NaCl and 0.2 mM $NaHCO_3$), 5 mg/L PSNPs in the same electrolyte solution were introduced across the supported RBCm. No noticeable PSNP deposition took place as no negative frequency shift was observed. PSNPs had the ζ potential of -43 ± 1 mV (avg. ± std. dev.) at 1 mM NaCl and 0.2 mM $NaHCO_3$. Both RBCm and PSNPs carried negative surface charge and the electrostatic repulsion impeded the deposition of PSNPs on the SRBCm coating. On the contrary, in a control experiment the PLL layer was not covered by RBCm. As shown in Figure 3b, when 5 mg/L PSNPs in 1 mM NaCl and 0.2 mM $NaHCO_3$ was introduced into the measurement chamber, PSNPs readily attached to the positively charged PLL layer with a favorable deposition rate of -2.48 ± 0.08 (avg. ± std. dev.) Hz/min due to electrostatic attraction. The contrast between Figure 3a and 3b indicates that there was a complete coverage of RBCm on the PLL-coated surface regarding ~100 nm or larger NPs. For the researchers who are interested in the NPs much smaller than 100 nm, biomacromolecules, or drug molecules, similar tests for complete coverage may be needed in case there are unexpected defects in SRBCm.

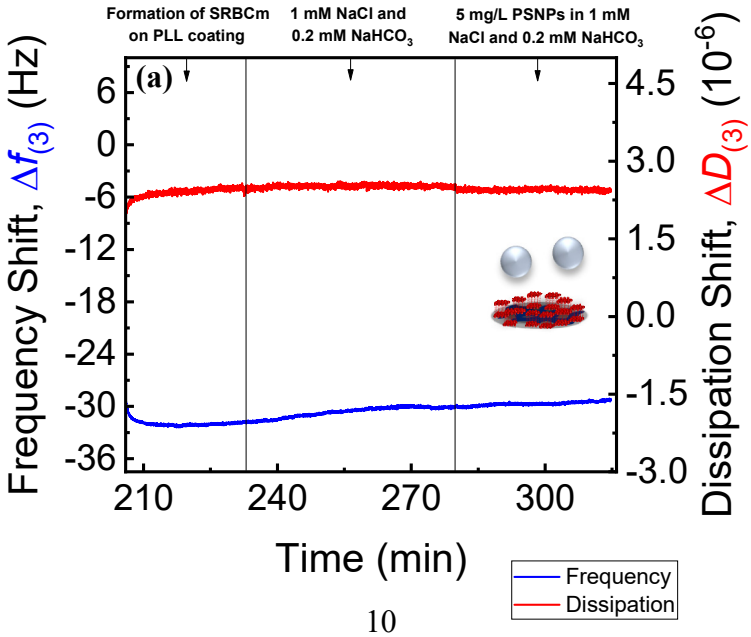

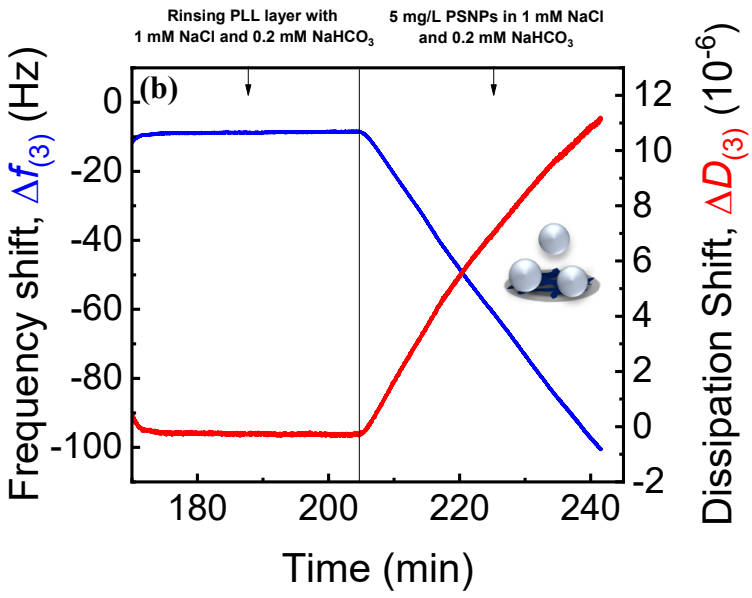

Figure 3. Deposition of 5 mg/L PSNPs on (a) supported RBCm-PLL-modified surface and (b) PLL-modified sensor surface in a background solution of 1 mM NaCl and 0.2 mM $NaHCO_3$. The contrast between no deposition on RBCm and favorable deposition of PSNPs on PLL indicated the complete coverage of SRBCm on PLL-modified surface regarding ~100 nm or larger NPs. The complete experimental data of (a) are shown in Figure S5a, Supporting Information (SI).

Characterization of Surface Morphology of Supported RBCm using AFM. AFM images of the surface morphology of a supported RBCm on the silica crystal sensor of QCM-D has been obtained in a solution of 1 mM NaCl and 0.2 mM $NaHCO_3$. In Figure 4a and 4c, the surface morphology of the SRBCm is shown in two-dimensional (2D), and three-dimensional (3D) AFM images, respectively. A control AFM image of the bare surface of a silica crystal sensor was obtained in DI water, as shown in Figure 4d in which the inherent surface roughness of ~10 nm on the bare silica surface can be observed. Figure 4a and 4c show that most area of SRBCm had the height of a few nanometers whereas there were also many protrusions (height: 30–50 nm) which were likely the aggregates of RBCm fragments embedded in or deposited on the SRBCm. The aggregates had the oval or dumbbell-like shape with the size (i.e., longest diameter) ranging from 150 nm to 1500 nm (Figure 4b), the average of which (i.e., 420 nm) is consistent with the average hydrodynamic diameter (i.e., 390 nm) of RBCm aggregates measured by DLS. The size range of 0.15-0.30 μm had the maximum number of RBCm aggregates, 54, out of the total, 129. The imaged

SRBCm and aggregates of RBCm were stable upon repeated imaging and no lateral movement was detected.

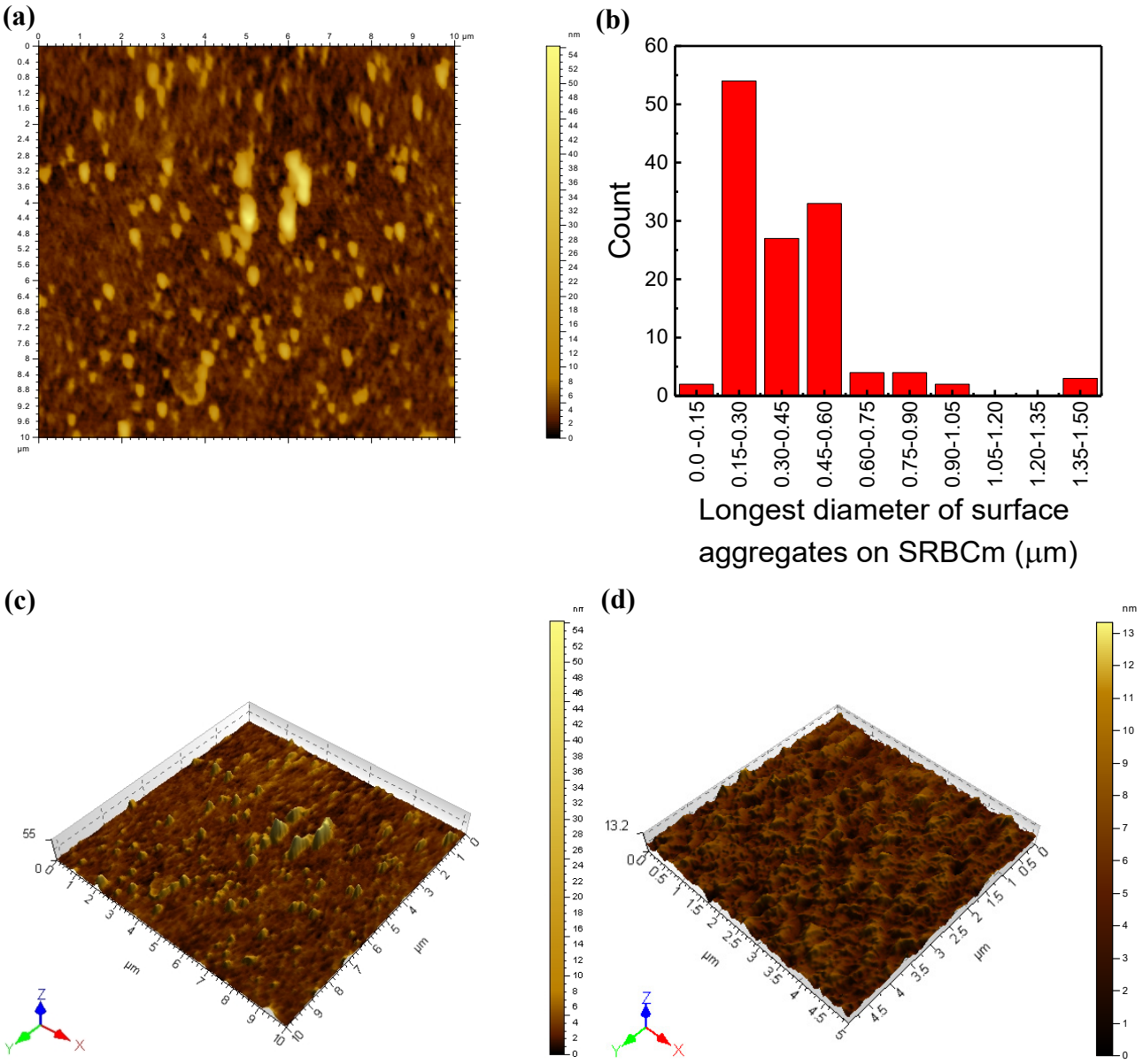

Figure 4. Characterization of surface morphology of a supported RBCm on a silica crystal sensor of QCM-D in a solution of 1 mM NaCl and 0.2 mM $NaHCO_3$. (a) 2D AFM image of supported RBCm. (b) Size distribution of RBCm aggregates on SRBCm based on the 2D AFM images shown in Figures 4a. (c) 3D AFM image of supported RBCm. (d) 3D AFM image of the bare surface of a QCM-D silica crystal sensor in DI water.

Characterization of Membrane Proteins on SRBCm using Immunofluorescence Microscopy (IFM). In order to test whether the surface of SRBCm retain the biological feature of the membrane of original erythrocytes, the distribution of surface proteins of erythrocytes on the surface of SRBCm was analyzed by indirect IFM. In these experiments, transparent glass slides were used as the substitutes of opaque silica crystal sensors for optical microscopy. To form SRBCm, the glass slide surface was incubated in 0.1 g/L PLL in HEPES buffer for 20 min and subsequently in the suspension of RBCm fragments in 1 mM NaCl and 0.2 mM $NaHCO_3$ for 30 min. Then, the surface of glass slide was incubated sequentially in the solutions of bovine serum albumin (BSA) for blocking non-specific binding of antibodies, primary rabbit anti-RBC antibody, and secondary antibody of donkey anti-rabbit conjugated with the fluorophore Alexa Fluor (AF) 594. During the incubation the surface proteins of erythrocytes would have been labeled by AF 594 if there was any on SRBCm. AF 594 is a bright, red-fluorescent dye upon excitation at 561 nm or 594 nm wavelength. Thus, the membrane proteins of erythrocytes would show red color under the microscope when excited. The intact red blood cells were used in place of SRBCm as the positive control. As shown in Figure 5b, surface proteins expressed on intact red blood cells exhibited red color under a confocal fluorescent microscope. In contrast, BSA was deposited on the PLL-modified glass slide for the negative control which showed no red color (Figure 5c). In Figure 5a, the well distributed red dots and clusters are the evidence that the surface proteins of erythrocytes were retained and properly distributed over the surface of SRBCm.

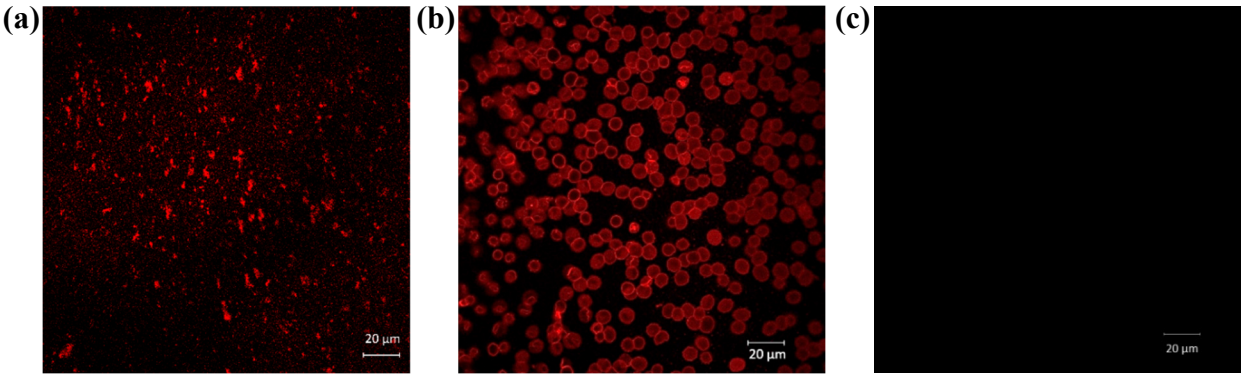

Figure 5: Immunofluorescence microscopy (IFM) images of erythrocyte surface proteins on (a) supported RBCm, (b) deposited intact erythrocytes as the positive control, and (c) bovine serum albumin coating as the negative control. Glass slides were used as the substitutes of silica crystal sensors to serve as the transparent substrates of all three layers above.

Deposition Kinetics and Attachment Efficiency of Model Positively Charged Nanoparticles on Supported RBCm. HemNPs were used as the model positively charged nanoparticles and 1 mM NaCl was used as the electrolyte concentration during deposition for method demonstration only. To quantify the probability of HemNPs attaching to erythrocyte membranes upon collision, the deposition attachment efficiency (α_D) of HemNPs on SRBCm was derived through QCM-D deposition experiments on both SRBCm and bare silica surface. The HemNPs suspended in the solution of 1 mM NaCl (pH 5.1 adjusted by 10 μM HCl), had the ζ potential of 14.6 ± 3.2 mV (avg. ± std. dev.) and the hydrodynamic diameter of 83–160 nm right before the deposition experiments. The point of zero charge (PZC) of HemNPs was pH 6.0 at 1 mM NaCl.[65] Figure 6a and 6b show the representative normalized frequency shifts, $\Delta f_{(3)}$, and dissipation shifts, $\Delta D_{(3)}$, of the third harmonic during deposition experiments of HemNPs on SRBCm. A SRBCm was first developed on the PLL-modified silica surface as described before. Then, the SRBCm was rinsed with the solutions of 1 mM NaCl and 0.2 mM $NaHCO_3$ (pH 7.0) and 1 mM NaCl (pH 5.1), sequentially, until the normalized frequency and dissipation responses were stabilized. Afterwards, 8.8 mg/L HemNPs suspended in 1 mM NaCl was introduced into the measurement chamber. Since RBCm fragments in 1 mM NaCl (pH 5.1) had the negative zeta potential of -0.78 ± 0.73 mV (avg. ± std. dev.), deposition occurred when the positively charged HemNPs approached the negatively charged SRBCm surface. The shift rate of $\Delta f_{(3)}$ during the initial 2.3 to 5 min deposition of HemNPs on SRBCm was -0.73 ± 0.40 Hz/min (avg. ± std. dev.), based on five experiments including Figure 6a, 6b, S3, and S4. The deposition of the positively charged HemNPs on negatively charged silica surface was conducted as favorable deposition experiments during which the attachment probability of HemNPs was 100% due to the electrostatic attraction between particles and surfaces. As shown in Figure 6c, when the favorable deposition of 8.8 mg/L HemNPs took place, a sharp decrease in $\Delta f_{(3)}$ and a concurrent quick increase in $\Delta D_{(3)}$ were observed. The shift rate of $\Delta f_{(3)}$ during the initial 5 mins of favorable deposition was determined to be -0.74 ± 0.43 Hz/min (avg. ± std. dev.) from triplicate experiments including Figure 6c. Since frequency shift is proportional to the deposited mass of NPs,[58] α_D was calculated using a classic methodology[57, 59] by taking the ratio of shift rate of frequency during the deposition on the SRBCm (i.e., -0.73 Hz/min) to that during the favorable deposition on silica (i.e., -0.74 Hz/min), as shown by Eq. 1 in the section of Materials and Methods. The α_D of HemNPs at 1 mM NaCl and pH 5.1, was thus determined as 0.99 ± 0.45 (avg. ± std. dev.), as shown in Figure 6d. The large standard

deviation of α_D is partially due to the inherent difference in the colloidal stability of 8.8 mg/L HemNPs since the deposition rate is lower when the NPs are less stable to aggregation.[59] Another possible reason for the large standard deviation of α_D is the variation of RBCm aggregates present on different SRBCm. Removal of RBCm aggregates from the RBCm suspension through filtration or centrifugation in future studies may improve the consistency of surface morphology of SRBCm and α_D.

As the deposition of HemNPs proceeded beyond the initial a few minutes, two types of deposition behavior were observed depending on the aggregation propensity of HemNPs which can be quantified by aggregation attachment efficiency (α_A). The α_A of HemNPs was derived using a classic methodology as detailed in SI and calculated using Eq. S2.[57, 66] Briefly, the α_A at 1 mM NaCl (pH 5.1) is the ratio of initial rate of increase in hydrodynamic diameter ($D_h(t)$) of HemNPs at 1 mM NaCl to that under favorable aggregation condition, usually at high electrolyte concentrations, in this case at NaCl concentration higher than 100 mM (Figure S2, SI).

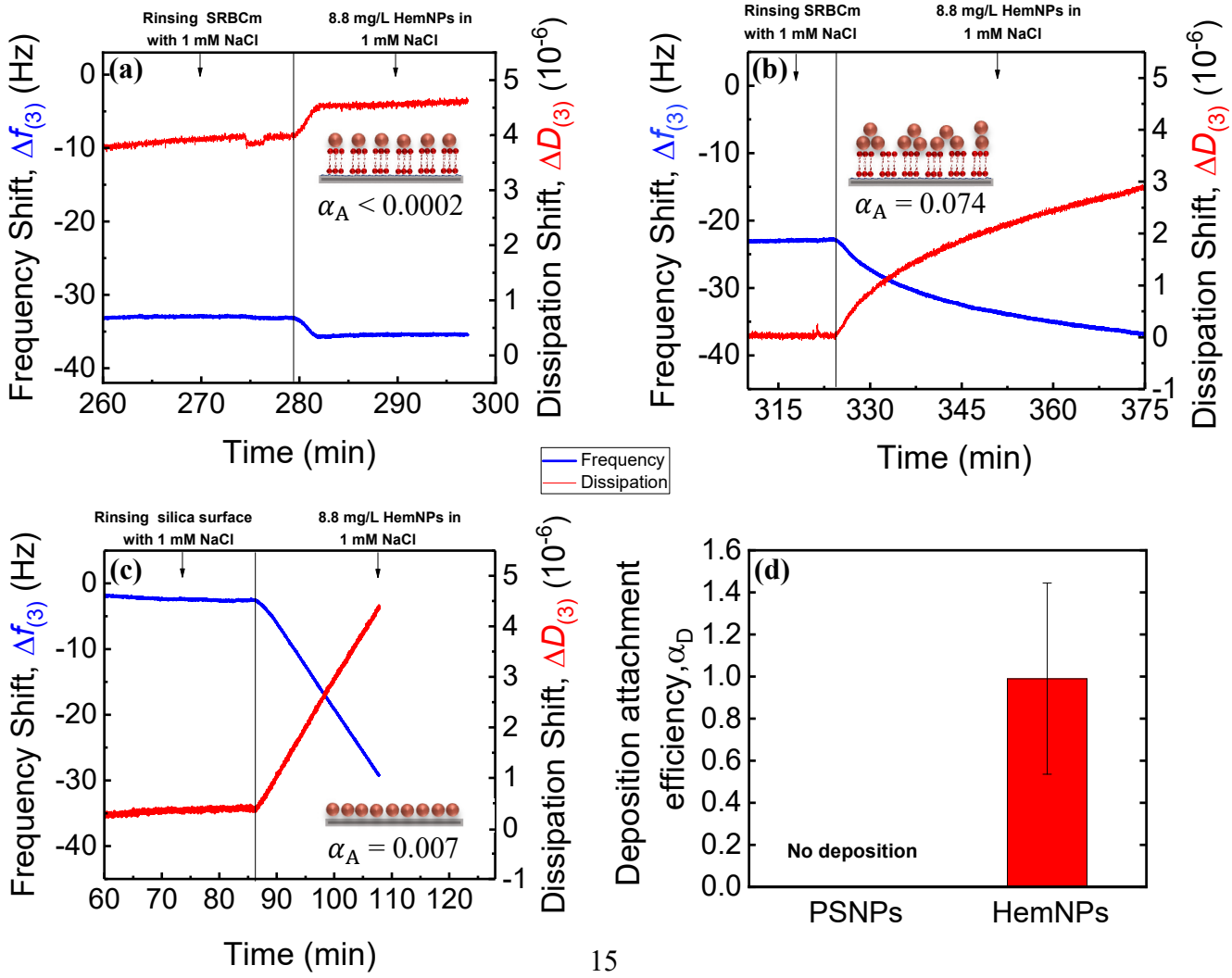

Figure 6. Frequency shift, $\Delta f_{(3)}$ and dissipation shift, $\Delta D_{(3)}$ during deposition of 8.8 mg/L HemNPs on SRBCm when (a) α_A< 0.0002 and (b) α_A = 0.074 and (c) on bare silica sensor, all at 1 mM NaCl and pH 5.1. (d) Deposition attachment efficiencies (α_D) on SRBCm of 5 mg/L PSNPs at 1 mM NaCl and 0.2 mM $NaHCO_3$ (pH 7.0) and 8.8 mg/L HemNPs at 1 mM NaCl (pH 5.1). The error bar represents the standard deviation.

The change in the aggregation attachment efficiency could result in significant difference in the deposition behavior of HemNPs on SRBCm. The variation of α_A was likely due to the inherent differences in the colloidal stability of different batches of 8.8 mg/L HemNPs. When $\alpha_A \leq 0.0002$, HemNPs had almost no propensity to attach to each other. As shown in Figure 6a for one of duplicate experiments (α_A = -0.0032 due to the slight negative drifting of DLS measurements), $\Delta f_{(3)}$ dropped quickly and reached a plateau at the frequency shift of -1.96 ± 0.84 Hz (avg. ± std. dev.) within 3 min, indicating that HemNPs quickly saturated all the available sites on SRBCm. Another duplicate result (α_A = 0.0002) with the data of the entire deposition experiment of HemNPs on SRBCm is presented in Figure S3, SI. It is likely that HemNPs formed a monolayer on the SRBCm and no multilayer deposition occurred since HemNPs could not attach to other HemNPs at such low α_A, as illustrated by the cartoon in Figure 6a. The $|\Delta D_{(3)}/\Delta f_{(3)}|$ of the HemNP monolayer on SRBCm was 0.23 ± 0.02×10^{-6} Hz^{-1} (avg. ± std. dev.) suggesting its viscoelasticity.[67]

When α_A was in the range of 0.074 to 0.173, HemNPs had noticeable propensity, although still low, to attach to other HemNPs at 1 mM NaCl, and continuous deposition of HemNPs was observed on SRBCm. As shown in Figure 6b, the deposition of HemNPs (α_A= 0.074) did not have a plateau even after the frequency shift due to deposition reached -17 Hz in a long duration (ca. 81 min). A complete QCM-D data of a duplicate deposition experiment of HemNPs (α_A= 0.173) on SRBCm is shown in Figure S4, SI. The continuous deposition of HemNPs was possibly due to the multilayer deposition of HemNPs on SRBCm, as illustrated by the cartoon in Figure 6b. We speculate that after the saturation of the surface of SRBCm by the first layer of HemNPs, the following HemNPs were able to attach to the first layer NPs. As this multilayer deposition proceeded, $\Delta f_{(3)}$ kept decreasing and $\Delta D_{(3)}$ kept increasing.

Deposition Kinetics and Attachment Efficiency of Model Negatively Charged Nanoparticles on Supported RBCm. Carboxylated polystyrene NPs were used as the model negatively charged NPs. The α_D of 5 mg/L PSNPs on SRBCm at 1 mM NaCl and 0.2 mM $NaHCO_3$ (pH 7.0) has been derived using the methodology similar to that for HemNPs and the data presented in Figure 3a and 3b, and their respective duplicate experiments. As shown by Figure 3a, no frequency decrease was observed when 5 mg/L PSNPs flowed across SRBCm indicating no deposition of PSNPs upon the collisions with SRBCm. Figure S5 in SI presents the entire frequency and dissipation data for the QCM-D experiment shown in Figure 3a and the duplicate experiment, both of which show no deposition or $\alpha_D = 0$ (Figure 6d). One of the reasons for no deposition of PSNPs on SRBCm was the electrostatic repulsion between them since both were negatively charged. Moreover, as the head groups of phospholipids are highly hydrophilic, water layers may have formed on the SRBCm resulting in repulsive hydration force which may have also deterred the attachment of PSNPs to SRBCm.[68-70]

CONCLUSION

In this work, we have successfully developed supported red blood cell membranes (SRBCm) on QCM-D piezoelectric sensors in aqueous solution at room temperature. Membranes of RBCs were isolated from whole blood and well dispersed. The hydrodynamic diameter of the dispersed membrane fragments was 390 ± 90 nm and their zeta potentials were -0.53 ± 0.41 mV at 1 mM NaCl and 0.2 mM $NaHCO_3$, pH 7.0. The formation of SRBCm was achieved mainly through the deposition of RBCm fragments on the PLL-modified silica crystal sensor under the above solution chemistry. The frequency shift of -26.2 ± 4.1 Hz and the low ratio of dissipation to frequency shift ($7.2 \pm 1.5\times10^{-8}$ Hz^{-1}) suggests a thin and rigid membrane layer comprised of a monolayer of flattened fragments of erythrocyte membranes. The complete coverage of SRBCm on the sensor was indicated by the plateau of frequency in the SRBCm formation stage and no deposition of polystyrene nanoparticles on SRBCm. The AFM surface morphology of SRBCm showed that aggregates of RBCm with the mean size of 420 nm were present on SRBCm. Indirect immunofluorescence microscopy showed that the erythrocyte surface proteins were adequately distributed on SRBCm. The deposition attachment efficiencies (α_D) of model nanoparticles, namely positively charged HemNPs and negatively charged PSNPs, on SRBCm were obtained at 1 mM NaCl (pH 5.1) and 1 mM NaCl and 0.2 mM $NaHCO_3$ (pH 7.0), respectively, for method

demonstration only. While PSNPs did not have any deposition, HemNPs experienced favorable deposition on SRBCm due to electrostatic attraction. The HemNPs with negligible aggregation propensity ($\alpha_A \leq 0.0002$) quickly saturated the surface of SRBCm whereas the HemNPs with noticeable aggregation propensity ($\alpha_A = 0.074$ or 0.173) had continuous deposition on SRBCm possibly due to multilayer deposition.

MATERIALS AND METHODS

Preparation and Characterization of Hematite Nanoparticles (HemNPs) and Carboxylated Polystyrene Nanoparticles (PSNPs). The 4.4 g/L of HemNP stock suspension was synthesized through forced hydrolysis of $FeCl_3$[71, 72] and used in a previous study[65] of our group. The TEM images show that the spherical HemNPs had an average size of 75 nm.[65] Before experiments, 8.8 mg/L HemNPs in 1 mM NaCl was prepared from the stock suspension and then sonicated in a bath sonicator (Branson M3800, USA; output power 120 W, frequency 40 kHz) for 30–60 minutes to break up aggregates of HemNPs. The carboxylated PSNPs with the average size of 107 nm were purchased from Polysciences, Inc.[65] 5 mg/L PSNPs in 1 mM NaCl and 0.2 mM $NaHCO_3$ (pH 7.0) were prepared for experiments and sonicated using the same bath sonicator for five minutes to break up aggregates.

The intensity-weighted hydrodynamic diameters of NPs were measured by dynamic light scattering (DLS) using a Zetasizer (Nano ZS90, Malvern Instruments, UK). 1 mL working suspension of NPs at the solution chemistry of interest was transferred into a transparent polystyrene cuvette (Sarstedt AG & Co. KG, Germany) for size measurement. The specifications of Zetasizer include scattering angle of 90°, measurement position in the center of the cell, accumulation time of 15 s for autocorrelation, and attenuation value as 10 or 11 to make scattered light intensity 150 to 350 kcps.

The zeta (ζ) potential of NPs was measured using a 'dip' cell kit (ZEN1002, Malvern, UK) and was calculated from the electrophoretic mobility using the Smoluchowski model. Three to five measurements were taken at 25 °C for NP samples.

Reagents and Solution Chemistry. All experiments were conducted at 25 °C, except for the preparation of RBCm suspension. NaCl and $NaHCO_3$ electrolyte stock solutions were prepared using ACS-grade chemicals (VWR, PA). A stock solution of 10 g/L cationic poly-L-lysine (PLL)

hydrobromide (P-1274, Sigma-Aldrich, St. Louis, MO) was prepared in HEPES buffer solution made up of 10 mM N-(2-hydroxyethyl) piperazine-N'-(2-ethanesulfonic acid) (HEPES) (H4034, Sigma-Aldrich, St. Louis, MO) and 100 mM NaCl. Both HEPES and PLL (molecular weight of 70,000-150,000) stock solutions were filtered through 0.2 μm polypropylene syringe filters (VWR, PA). All experiments with PSNPs were conducted at 1 mM NaCl and pH 7.0 buffered with 0.2 mM $NaHCO_3$. All experiments with HemNPs were conducted at 1 mM NaCl and pH 5.1 (adjusted by 10 μM HCl). All solutions were prepared with DI water (Millipore, MA) that had a resistivity of 18.2 MΩ·cm.

Preparation of Colloidal Suspension of RBCm Fragments from Human Blood. The whole blood (O negative) was purchased from the Continental Blood Bank (Fort Lauderdale, FL). The samples were preserved with dipotassium ethylenediaminetetraacetic acid (K_2EDTA) to prevent the coagulation of blood cells. At first, the RBC pellets were isolated from plasma by centrifuging (centrifuge 40R, Thermo Scientific, Danville, IN) the whole blood at 4 °C and 800 g for 10 min. The resulting precipitates of erythrocytes were collected and washed three times through centrifugation, withdrawing supernatants, and refilling with phosphate-buffered saline (PBS) (Amresco Inc., OH) at pH 7.4. Then, 4-time diluted PBS (0.25×PBS) was added to trigger hemolysis of erythrocytes (hypotonic treatment). The hemolyzed cell suspension was centrifuged at 2500 g and 4 °C for 10 min to separate the cellular contents (i.e., hemoglobin) from the RBC membranes. The supernatant was discarded via a micropipette. The process of refilling with 0.25×PBS, centrifugation, and discarding supernatant was repeated three times. The resulting RBC ghosts were further washed with DI water three times using the above process. Vortex was used to redisperse the settled RBC ghosts every time during washing with either 0.25×PBS or DI water. After washing with 0.25×PBS, less than 1 mL of pink RBC ghosts were produced; after DI water washing, RBC ghosts turned white in color as shown in Figure S1, SI. The centrifuge tubes containing white RBC ghosts in DI water were kept at 3˚C and allowed for static diffusion for 3 days until the erythrocyte membranes spontaneously dispersed into the DI water and formed the homogenous stock of RBCm suspension. To preserve the RBCm suspension for longer duration, they were stored at -20 ˚C. Approximately, 10 ml RBCm suspension was harvested from 6 ml whole blood resulting in the membrane concentration in RBCm suspension equal to 60% of that in whole blood. Before use, certain amounts of NaCl and $NaHCO_3$ stock solutions were added to

the 10 mL stock RBCm suspension to have 1 mM NaCl and 0.2 mM $NaHCO_3$ at pH 7.0. Then, the RBCm suspension was sonicated with probe sonicator (Q55, Qsonica, Newtown, CT) for ten cycles of 10 second sonication to further reduce the size of RBCm pieces. The photographs showing each step of preparing RBCm suspension from whole blood are shown in Figure S1, SI.

Quartz Crystal Microbalance with Dissipation Monitoring (QCM-D). The formation of SRBCm and the deposition of NPs on SRBCm were conducted using a QCM-D (E1, Q-Sense, Västra Frölunda, Sweden) with a QFM 401 flow module. A 5-MHz AT-cut quartz crystal sensor with SiO_2 surface (QSX 303, Q-Sense) was mounted in the module. Details on the cleaning of the measurement chamber and sensor surface, and the preparation of solutions are provided in the SI. For all QCM-D experiments, the sensor surface was first rinsed with DI water for 30 to 90 min until stable baselines were reached. Baselines of any solution were considered stable when the shifts in the normalized frequency and dissipation were less than 0.2 Hz and 0.15×10^{-6}, respectively, over a time period of 10 min. During the experiments, the flow rate was maintained at 0.1 mL/min controlled by a peristaltic pump (ISM935C, Ismatec, Wertheim, Germany). The temperature was maintained at 25 °C. All the experiments were repeated at least twice. The QCM-D data were analyzed with the help of QTools software.

In order to acquire the deposition kinetics of PSNPs and HemNPs on SRBCm in their corresponding electrolyte solution, both deposition experiments on SRBCm and favorable deposition experiments were performed. For deposition experiments on SRBCm, the crystal surface was first coated by PLL by successively rinsing the surface with HEPES buffer, 0.1 g/L PLL solution, and additional HEPES buffer. During the PLL adsorption process, there were sharp decrease and increase of the frequency and dissipation, respectively, until they reached a plateau suggesting the crystal surface was completely coated with PLL.[58, 66] Then, the PLL layer was covered by SRBCm as described before. After rinsing with the corresponding background solution, NP suspension was introduced into the measurement chamber for the deposition of NPs on SRBCm. The favorable deposition experiments of positively charged HemNPs was conducted on bare silica surface. The negatively charged silica surface was rinsed by 1 mM NaCl (pH 5.1) for stable baselines. Then, the HemNPs suspension was directed across the silica surface for deposition to occur at 1 mM NaCl (pH 5.1). For PSNPs, the favorable deposition was conducted on PLL-modified silica surface at 1 mM NaCl and 0.2 mM $NaHCO_3$ (pH 7.0).

The probability of HemNPs and PSNPs attaching to SRBCm upon collision was quantified using the deposition attachment efficiency, α_D. Since the shift of frequency was found to be proportional to the mass of deposited NPs,[58] α_D was calculated by taking the raito of the initial rates of normalized frequency shift ($d\Delta f_{(3)}/dt$) during NP deposition on SRBCm to the $(d\Delta f_{(3)}/dt)_{fav}$ during the favorable deposition at the same solution chemistry:[39, 59]

$$\alpha_D = \frac{\frac{d\Delta f_{(3)}}{dt}}{(\frac{d\Delta f_{(3)}}{dt})_{fav}} \quad (1)$$

Cryogenic Transmission Electron Microscopy (Cryo-TEM). Cryo-TEM imaging was employed to examine the RBCm fragments in the erythrocyte membrane suspension at 1 mM NaCl and 0.2 mM $NaHCO_3$. Three microliters of the suspension were applied to carbon grids (Protochips, Inc., Morrisville, NC) and vitrified using a Vitrobot (Mark IV, FEI Co., Hillsboro, OR) which operated at 4°C and ~90% humidity in the control chamber. Then, the vitrified sample was stored under liquid nitrogen and transferred into a cryo-holder (Model 626/70, Gatan, Inc., Pleasanton, CA) for imaging. The sample was inspected using a camera (4k × 4k CCD, Gatan, Inc., Pleasanton, CA) on a TEM (Tecnai G2 F20-TWIN, FEI Co., Hillsboro, OR) operated at a voltage of 200 kV using low dose conditions (~20 e/Å^2). Images were recorded with a defocus of approximately -3 μm to improve contrast.

Atomic Force Microscopy (AFM) Imaging. AFM imaging of SRBCm and bare silica surface were performed using an atomic force microscope (5420, Agilent Technologies, Inc, Santa Clara, CA) in aqueous solutions (i.e., RBCm suspension for SRBCm or DI water for silica surface). A cleaned silica quartz crystal sensor was soaked in 0.1 g/L PLL in HEPES buffer for 20 min and then subsequently soaked in RBCm suspension at 1 mM NaCl and 0.2 mM $NaHCO_3$ for at least 30 min to form SRBCm on the PLL-modified sensor before observation. Bare silica surface was just soaked in DI water for imaging. The petri dish with the prepared sensor in the respective solution was mounted on the stage of AFM. Triangular silicon nitride cantilever with a nominal spring constant of 0.088 N/m (HYDRA4V-100NG, Applied Nanostructures, Inc., Mountain View, CA) was mounted in the AFM cell. The images were acquired in AC mode with 30 % drive, a scanning speed of 2.02 in/s, and manual tuning. The images were further processed using Pico image tool.

Immunofluorescence Microscopy (IFM) of Supported RBCm. Due to the opacity of silica quartz crystal sensors, pre-cleaned microscopic glass slides (Inkjet, Fisher brand™, Hampton, NH) were used instead as an amorphous silica substrate for the indirect immunofluorescence (IF) imaging. For SRBCm, positive control (i.e., intact erythrocytes), and negative control (i.e., bovine serum albumin, BSA), the surface of glass slide was first incubated with 0.1 g/L PLL in HEPES buffer for 20 min and then with corresponding samples, i.e., RBCm suspension, RBCs in Roswell Park Memorial Institute (RPMI) medium, and 2% BSA in PBS, respectively, for 30 min at room temperature. PLL and sample solutions were removed from the slide using a micropipette after incubation. Afterwards, the glass slide was then incubated in BSA solution at 37 ℃ for 30 min, as a blocking process to prevent non-specific binding of antibodies to the sample surfaces in the following steps. Then, the glass slide was successively incubated with the solution of 1°Ab, i.e., primary rabbit anti-human RBC antibody (Cat# 209-4139, Rockland) diluted by 1000 times in 5% donkey serum, and the solution of 2°Ab, i.e., secondary antibody of donkey anti-Rabbit Immunoglobulin G Alexa Fluor (AF) 594 (Cat# 711-585-152, Jackson ImmunoResearch Laboratories, Inc.) diluted by 100 times in 5% donkey serum, both at 37 ℃ for 60 min. The glass slides were washed with PBS for three times after the incubation with BSA, 1°Ab, and 2°Ab. For the negative control, 5% donkey serum was used instead of 1°Ab. Images were acquired through a confocal laser scanning microscope (Zeiss, Pleasanton, CA) with 63× (oil) objective and ZEN software was used to process the raw images.

ACKNOWLEDGEMENTS

This research was supported by Florida Atlantic University (FAU). We thank Dr. Kai Loon Chen for the donation of hematite nanoparticles and Dr. Waseem Asghar, Department of Electrical Engineering and Computer Science, FAU, for letting us use the centrifuge. We acknowledge Paul R. Chipman and Rodolfo Alvarado, Electron Microscopy Core, Interdisciplinary Center for Biotechnology Research, University of Florida (Gainesville, FL) for performing cryo-TEM imaging. We also acknowledge Shirin Cupples for her unsuccessful attempts on making SRBCm.

ASSOCIATED CONTENT

Supporting Information

Additional information on materials and methods; Photographs at each step of the preparation of RBCm suspension (Figure S1); aggregation attachment efficiencies of HemNPs as a function of NaCl concentration at pH 5.1 (Figure S2); complete profiles of frequency and dissipation of a QCM-D deposition experiment of 8.8 mg/L HemNPs (α_A = 0.0002) on SRBCm at 1 mM NaCl (pH 5.1), as a duplicate experiment for 'Figure 6a' (Figure S3); a complete frequency and dissipation profile during a QCM-D deposition experiment of 8.8 mg/L HemNPs (α_A = 0.173) on SRBCm at 1 mM NaCl (pH 5.1) which is a duplicate experiment for 'Figure 6b' (Figure S4); The entire frequency and dissipation profiles of QCM-D deposition experiments of 5 mg/L PSNPs on SRBCm at 1 mM NaCl and 0.2 mM $NaHCO_3$ (pH 7.0) (Figure S5).

COMPETING INTERESTS

The authors declare no competing non-financial interests but the following competing financial interests: a patent application was filed for the supported erythrocyte membranes.

REFERENCES

1. Estelrich, J.; Sanchez-Martin, M. J.; Busquets, M. A., Nanoparticles in magnetic resonance imaging: from simple to dual contrast agents. *Int J Nanomedicine* **2015,** *10*, 1727-41.
2. Weissig, V.; Pettinger, T. K.; Murdock, N., Nanopharmaceuticals (part 1): products on the market. *Int J Nanomedicine* **2014,** *9*, 4357-73.
3. Lu, M.; Cohen, M. H.; Rieves, D.; Pazdur, R., FDA report: Ferumoxytol for intravenous iron therapy in adult patients with chronic kidney disease. *Am J Hematol* **2010,** *85*, (5), 315-9.
4. Ventola, C. L., Progress in Nanomedicine: Approved and Investigational Nanodrugs. *P T* **2017,** *42*, (12), 742-755.
5. Gupta, R.; Xie, H., Nanoparticles in Daily Life: Applications, Toxicity and Regulations. *J Environ Pathol Toxicol Oncol* **2018,** *37*, (3), 209-230.
6. Kim, K. T.; Eo, M. Y.; Nguyen, T. T. H.; Kim, S. M., General review of titanium toxicity. *Int J Implant Dent* **2019,** *5*, (1), 10.
7. Kessler, R., Engineered nanoparticles in consumer products: understanding a new ingredient. *Environ Health Perspect* **2011,** *119*, (3), a120-5.
8. Contini, C.; Schneemilch, M.; Gaisford, S.; Quirke, N., Nanoparticle–membrane interactions. *Journal of Experimental Nanoscience* **2017,** *13*, (1), 62-81.
9. Souza, V. G. L.; Fernando, A. L., Nanoparticles in food packaging: Biodegradability and potential migration to food-A review. *Food Packaging Shelf* **2016,** *8*, 63-70.
10. He, X.; Hwang, H. M., Nanotechnology in food science: Functionality, applicability, and safety assessment. *J Food Drug Anal* **2016,** *24*, (4), 671-681.

11. Stearns, R. C.; Paulauskis, J. D.; Godleski, J. J., Endocytosis of ultrafine particles by A549 cells. *Am J Respir Cell Mol Biol* **2001,** *24*, (2), 108-15.
12. Sukhanova, A.; Bozrova, S.; Sokolov, P.; Berestovoy, M.; Karaulov, A.; Nabiev, I., Dependence of Nanoparticle Toxicity on Their Physical and Chemical Properties. *Nanoscale Res Lett* **2018,** *13*, (1), 44.
13. Miller, M. R.; Raftis, J. B.; Langrish, J. P.; McLean, S. G.; Samutrtai, P.; Connell, S. P.; Wilson, S.; Vesey, A. T.; Fokkens, P. H. B.; Boere, A. J. F.; Krystek, P.; Campbell, C. J.; Hadoke, P. W. F.; Donaldson, K.; Cassee, F. R.; Newby, D. E.; Duffin, R.; Mills, N. L., Inhaled Nanoparticles Accumulate at Sites of Vascular Disease. *ACS Nano* **2017,** *11*, (5), 4542-4552.
14. Miller, M. R.; McLean, S. G.; Duffin, R.; Lawal, A. O.; Araujo, J. A.; Shaw, C. A.; Mills, N. L.; Donaldson, K.; Newby, D. E.; Hadoke, P. W., Diesel exhaust particulate increases the size and complexity of lesions in atherosclerotic mice. *Part Fibre Toxicol* **2013,** *10*, 61.
15. Donaldson, K.; Tran, L.; Jimenez, L. A.; Duffin, R.; Newby, D. E.; Mills, N.; MacNee, W.; Stone, V., Combustion-derived nanoparticles: a review of their toxicology following inhalation exposure. *Part Fibre Toxicol* **2005,** *2*, 10.
16. Oberdorster, G. S., Z.; Atudorei, V.; Elder, A.; Gelein, R.;Lunts, A.; Kreyling, W.; Cox, C. , Extrapulmonary translocation of ultrafine carbon particles following whole-body inhalation exposure of rats. . *J. Toxicol. Environ. Health, Part A 2002, 65, 1531−1543* **2002,** *65*, (20), 1531-43.
17. Hirn, S.; Semmler-Behnke, M.; Schleh, C.; Wenk, A.; Lipka, J.; Schaffler, M.; Takenaka, S.; Moller, W.; Schmid, G.; Simon, U.; Kreyling, W. G., Particle size-dependent and surface charge-dependent biodistribution of gold nanoparticles after intravenous administration. *Eur J Pharm Biopharm* **2011,** *77*, (3), 407-16.
18. Nel, A.; Xia, T.; Madler, L.; Li, N., Toxic potential of materials at the nanolevel. *Science* **2006,** *311*, (5761), 622-7.
19. Li, S. Q.; Zhu, R. R.; Zhu, H.; Xue, M.; Sun, X. Y.; Yao, S. D.; Wang, S. L., Nanotoxicity of TiO_2 nanoparticles to erythrocyte in vitro. *Food Chem Toxicol* **2008,** *46*, (12), 3626-31.
20. Shang, L.; Nienhaus, K.; Nienhaus, G. U., Engineered nanoparticles interacting with cells: size matters. *J Nanobiotechnology* **2014,** *12*, 5.
21. Oberdorster, G.; Oberdorster, E.; Oberdorster, J., Nanotoxicology: an emerging discipline evolving from studies of ultrafine particles. *Environ Health Perspect* **2005,** *113*, (7), 823-39.
22. Miller, M. R.; Raftis, J. B.; Langrish, J. P.; McLean, S. G.; Samutrtai, P.; Connell, S. P.; Wilson, S.; Vesey, A. T.; Fokkens, P. H. B.; Boere, A. J. F.; Krystek, P.; Campbell, C. J.; Hadoke, P. W. F.; Donaldson, K.; Cassee, F. R.; Newby, D. E.; Duffin, R.; Mills, N. L., Correction to "Inhaled Nanoparticles Accumulate at Sites of Vascular Disease". *ACS Nano* **2017,** *11*, (10), 10623-10624.
23. Villa, C. H.; Anselmo, A. C.; Mitragotri, S.; Muzykantov, V., Red blood cells: Supercarriers for drugs, biologicals, and nanoparticles and inspiration for advanced delivery systems. *Adv Drug Deliv Rev* **2016,** *106*, (Pt A), 88-103.
24. Chen, L. Q.; Fang, L.; Ling, J.; Ding, C. Z.; Kang, B.; Huang, C. Z., Nanotoxicity of silver nanoparticles to red blood cells: size dependent adsorption, uptake, and hemolytic activity. *Chem Res Toxicol* **2015,** *28*, (3), 501-9.
25. de la Harpe, K. M.; Kondiah, P. P. D.; Choonara, Y. E.; Marimuthu, T.; du Toit, L. C.; Pillay, V., The Hemocompatibility of Nanoparticles: A Review of Cell-Nanoparticle Interactions and Hemostasis. *Cells* **2019,** *8*, (10).

26. Cruz, G. G. d. l.; Rodríguez-Fragoso, P.; Reyes-Esparza, J.; Rodriguez-López, A. M.; Gómez-Cansino, R.; Rodríguez-Fragoso, L. Interaction of Nanoparticles with Blood Components and Associated Pathophysiological Effects. In *Unraveling the Safety Profile of Nanoscale Particles and Materials*, Andreia, C. G.; Marisa, P. S., Eds. IntechOpen: Rijeka, 2017; p Ch. 3.
27. Zhang, X. F.; Yang, S. H., Nonspecific Adsorption of Charged Quantum Dots on Supported Zwitterionic Lipid Bilayers: Real-Time Monitoring by Quartz Crystal Microbalance with Dissipation. *Langmuir* **2011,** *27*, (6), 2528-2535.
28. Nel, A. E.; Madler, L.; Velegol, D.; Xia, T.; Hoek, E. M. V.; Somasundaran, P.; Klaessig, F.; Castranova, V.; Thompson, M., Understanding biophysicochemical interactions at the nano-bio interface. *Nat Mater* **2009,** *8*, (7), 543-557.
29. Wottrich, R.; Diabate, S.; Krug, H. F., Biological effects of ultrafine model particles in human macrophages and epithelial cells in mono- and co-culture. *Int J Hyg Environ Health* **2004,** *207*, (4), 353-61.
30. Wahab, R.; Khan, F.; Al-Khedhairy, A. A., Hematite iron oxide nanoparticles: apoptosis of myoblast cancer cells and their arithmetical assessment. *RSC Advances* **2018,** *8*, (44), 24750-24759.
31. Hesler, M.; Aengenheister, L.; Ellinger, B.; Drexel, R.; Straskraba, S.; Jost, C.; Wagner, S.; Meier, F.; von Briesen, H.; Buchel, C.; Wick, P.; Buerki-Thurnherr, T.; Kohl, Y., Multi-endpoint toxicological assessment of polystyrene nano- and microparticles in different biological models in vitro. *Toxicol In Vitro* **2019,** *61*, 104610.
32. Abdelkhaliq, A.; van der Zande, M.; Punt, A.; Helsdingen, R.; Boeren, S.; Vervoort, J. J. M.; Rietjens, I.; Bouwmeester, H., Impact of nanoparticle surface functionalization on the protein corona and cellular adhesion, uptake and transport. *J Nanobiotechnology* **2018,** *16*, (1), 70.
33. Pan, D. C.; Myerson, J. W.; Brenner, J. S.; Patel, P. N.; Anselmo, A. C.; Mitragotri, S.; Muzykantov, V., Nanoparticle Properties Modulate Their Attachment and Effect on Carrier Red Blood Cells. *Sci Rep* **2018,** *8*, (1), 1615.
34. Zhao, Z.; Ukidve, A.; Gao, Y.; Kim, J.; Mitragotri, S., Erythrocyte leveraged chemotherapy (ELeCt): Nanoparticle assembly on erythrocyte surface to combat lung metastasis. *Sci Adv* **2019,** *5*, (11), eaax9250.
35. Brenner, J. S.; Pan, D. C.; Myerson, J. W.; Marcos-Contreras, O. A.; Villa, C. H.; Patel, P.; Hekierski, H.; Chatterjee, S.; Tao, J. Q.; Parhiz, H.; Bhamidipati, K.; Uhler, T. G.; Hood, E. D.; Kiseleva, R. Y.; Shuvaev, V. S.; Shuvaeva, T.; Khoshnejad, M.; Johnston, I.; Gregory, J. V.; Lahann, J.; Wang, T.; Cantu, E.; Armstead, W. M.; Mitragotri, S.; Muzykantov, V., Red blood cell-hitchhiking boosts delivery of nanocarriers to chosen organs by orders of magnitude. *Nat Commun* **2018,** *9*, (1), 2684.
36. Yoo, J. W.; Irvine, D. J.; Discher, D. E.; Mitragotri, S., Bio-inspired, bioengineered and biomimetic drug delivery carriers. *Nat Rev Drug Discov* **2011,** *10*, (7), 521-35.
37. Anselmo, A. C.; Gupta, V.; Zern, B. J.; Pan, D.; Zakrewsky, M.; Muzykantov, V.; Mitragotri, S., Delivering nanoparticles to lungs while avoiding liver and spleen through adsorption on red blood cells. *ACS Nano* **2013,** *7*, (12), 11129-37.
38. Rothen-Rutishauser, B. M.; Schurch, S.; Haenni, B.; Kapp, N.; Gehr, P., Interaction of fine particles and nanoparticles with red blood cells visualized with advanced microscopic techniques. *Environ Sci Technol* **2006,** *40*, (14), 4353-9.
39. Yi, P.; Chen, K. L., Interaction of Multiwalled Carbon Nanotubes with Supported Lipid Bilayers and Vesicles as Model Biological Membranes. *Environ Sci Technol* **2013,** *47*, (11), 5711-5719.

40. Liu, X. T.; Chen, K. L., Aggregation and interactions of chemical mechanical planarization nanoparticles with model biological membranes: role of phosphate adsorption. *Environmental Science: Nano* **2016,** *3*, (1), 146-156.
41. Yousefi, N.; Tufenkji, N., Probing the Interaction between Nanoparticles and Lipid Membranes by Quartz Crystal Microbalance with Dissipation Monitoring. *Frontiers in Chemistry* **2016,** *4*.
42. Gu, W.; Liu, X.; Yi, P., Influence of pH and electrolyte on the deposition of cerium oxide nanoparticles on supported lipid bilayers. *Environmental Science: Nano* **2022,** *9*, (6), 1986-1995.
43. Waldie, S.; Lind, T. K.; Browning, K.; Moulin, M.; Haertlein, M.; Forsyth, V. T.; Luchini, A.; Strohmeier, G. A.; Pichler, H.; Maric, S.; Cardenas, M., Localization of Cholesterol within Supported Lipid Bilayers Made of a Natural Extract of Tailor-Deuterated Phosphatidylcholine. *Langmuir* **2018,** *34*, (1), 472-479.
44. Luchini, A.; Nzulumike, A. N. O.; Lind, T. K.; Nylander, T.; Barker, R.; Arleth, L.; Mortensen, K.; Cardenas, M., Towards biomimics of cell membranes: Structural effect of phosphatidylinositol triphosphate (PIP3) on a lipid bilayer. *Colloids Surf B Biointerfaces* **2019,** *173*, 202-209.
45. Reviakine, I.; Simon, A.; Brisson, A., Effect of Ca^{2+} on the Morphology of Mixed DPPC−DOPS Supported Phospholipid Bilayers. *Langmuir* **2000,** *16*, (4), 1473-1477.
46. Hedegaard, S. F.; Derbas, M. S.; Lind, T. K.; Kasimova, M. R.; Christensen, M. V.; Michaelsen, M. H.; Campbell, R. A.; Jorgensen, L.; Franzyk, H.; Cardenas, M.; Nielsen, H. M., Fluorophore labeling of a cell-penetrating peptide significantly alters the mode and degree of biomembrane interaction. *Sci Rep* **2018,** *8*, (1), 6327.
47. Melby, E. S.; Mensch, A. C.; Lohse, S. E.; Hu, D.; Orr, G.; Murphy, C. J.; Hamers, R. J.; Pedersen, J. A., Formation of supported lipid bilayers containing phase-segregated domains and their interaction with gold nanoparticles. *Environmental Science: Nano* **2016,** *3*, (1), 45-55.
48. Himbert, S.; Alsop, R. J.; Rose, M.; Hertz, L.; Dhaliwal, A.; Moran-Mirabal, J. M.; Verschoor, C. P.; Bowdish, D. M.; Kaestner, L.; Wagner, C.; Rheinstadter, M. C., The Molecular Structure of Human Red Blood Cell Membranes from Highly Oriented, Solid Supported Multi-Lamellar Membranes. *Sci Rep* **2017,** *7*, 39661.
49. Kim, I.; Kwon, D.; Lee, D.; Lee, T. H.; Lee, J. H.; Lee, G.; Yoon, D. S., A highly permselective electrochemical glucose sensor using red blood cell membrane. *Biosensors and Bioelectronics* **2018,** *102*, 617-623.
50. Rakow, A. L.; Hochmuth, R. M., Effect of heat treatment on the elasticity of human erythrocyte membrane. *Biophys J* **1975,** *15*, (11), 1095-100.
51. Lepock, J. R., Protein Denaturation During Heat Shock. In *Thermobiology*, 1997; Vol. 19, pp 223-259.
52. Gershfeld, N. L.; Murayama, M., Thermal instability of red blood cell membrane bilayers: temperature dependence of hemolysis. *J Membr Biol* **1988,** *101*, (1), 67-72.
53. Tanaka, M.; Kaufmann, S.; Nissen, J.; Hochrein, M., Orientation selective immobilization of human erythrocyte membranes on ultrathin cellulose films. *Phys Chem Chem Phys* **2001,** *3*, (18), 4091-4095.
54. Ehrenhöfer, U; Rakowska, A; Schneider, S. W.; Schwab, A; Oberleithner, H. The atomic force microscope detects ATP-sensitive protein clusters in the plasma membrane of transformed MDCK cells. *Cell Biology International* **1997,** *21*, (11), 737-746.

55. Perez, J.-B.; Martinez, K. L.; Segura, J.-M.; Vogel, H., Supported Cell-Membrane Sheets for Functional Fluorescence Imaging of Membrane Proteins. *Adv Funct Mater* **2006,** *16*, (2), 306-312.
56. Avery, J.; Ellis, D. J.; Lang, T.; Holroyd, P.; Riedel, D.; Henderson, R. M.; Edwardson, J. M.; Jahn, R., A Cell-Free System for Regulated Exocytosis in Pc12 Cells. *J Cell Biol* **2000,** *148*, (2), 317-324.
57. Chen, K. L.; Elimelech, M., Aggregation and deposition kinetics of fullerene (C_{60}) nanoparticles. *Langmuir* **2006,** *22*, (26), 10994-11001.
58. Yi, P.; Chen, K. L., Influence of Surface Oxidation on the Aggregation and Deposition Kinetics of Multiwalled Carbon Nanotubes in Monovalent and Divalent Electrolytes. *Langmuir* **2011,** *27*, (7), 3588-3599.
59. Chen, K. L.; Elimelech, M., Interaction of Fullerene (C_{60}) Nanoparticles with Humic Acid and Alginate Coated Silica Surfaces: Measurements, Mechanisms, and Environmental Implications. *Environ Sci Technol* **2008,** *42*, (20), 7607-7614.
60. Cho, N. J.; Frank, C. W.; Kasemo, B.; Hook, F., Quartz crystal microbalance with dissipation monitoring of supported lipid bilayers on various substrates. *Nat Protoc* **2010,** *5*, (6), 1096-1106.
61. Richter, R. P.; Berat, R.; Brisson, A. R., Formation of solid-supported lipid bilayers: An integrated view. *Langmuir* **2006,** *22*, (8), 3497-3505.
62. Keller, C. A.; Kasemo, B., Surface specific kinetics of lipid vesicle adsorption measured with a quartz crystal microbalance. *Biophysical Journal* **1998,** *75*, (3), 1397-1402.
63. Richter, R.; Mukhopadhyay, A.; Brisson, A., Pathways of lipid vesicle deposition on solid surfaces: A combined QCM-D and AFM study. *Biophysical Journal* **2003,** *85*, (5), 3035-3047.
64. Svedhem, S.; Dahlborg, D.; Ekeroth, J.; Kelly, J.; Hook, F.; Gold, J., In situ peptide-modified supported lipid bilayers for controlled cell attachment. *Langmuir* **2003,** *19*, (17), 6730-6736.
65. Hussain, K. A.; Yi, P., Heteroaggregation of Neutral and Charged Nanoparticles: A Potential Method of Making Core–Shell Nanohybrids through Self-Assembly. *The Journal of Physical Chemistry C* **2020,** *124*, (35), 19282-19288.
66. Chen, K. L.; Mylon, S. E.; Elimelech, M., Aggregation kinetics of alginate-coated hematite nanoparticles in monovalent and divalent electrolytes. *Environ Sci Technol* **2006,** *40*, (5), 1516-1523.
67. Yi, P.; Chen, K. L., Influence of Solution Chemistry on the Release of Multiwalled Carbon Nanotubes from Silica Surfaces. *Environ Sci Technol* **2013,** *47*, (21), 12211-12218.
68. Higgins, M. J.; Polcik, M.; Fukuma, T.; Sader, J. E.; Nakayama, Y.; Jarvis, S. P., Structured water layers adjacent to biological membranes. *Biophys J* **2006,** *91*, (7), 2532-42.
69. Berkowitz, M. L.; Vacha, R., Aqueous solutions at the interface with phospholipid bilayers. *Acc Chem Res* **2012,** *45*, (1), 74-82.
70. Berkowitz, M. L.; Bostick, D. L.; Pandit, S., Aqueous solutions next to phospholipid membrane surfaces: insights from simulations. *Chem Rev* **2006,** *106*, (4), 1527-39.
71. Mylon, S. E.; Chen, K. L.; Elimelech, M., Influence of natural organic matter and ionic composition on the kinetics and structure of hematite colloid aggregation: implications to iron depletion in estuaries. *Langmuir* **2004,** *20*, (21), 9000-6.
72. Huynh, K. A.; McCaffery, J. M.; Chen, K. L., Heteroaggregation of Multiwalled Carbon Nanotubes and Hematite Nanoparticles: Rates and Mechanisms. *Environ Sci Technol* **2012,** *46*, (11), 5912-5920.

TOC ART

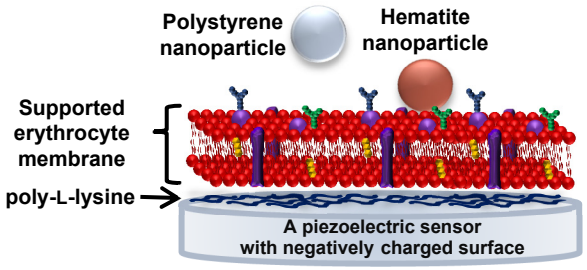

Supporting Information

Supported Erythrocyte Membranes on Piezoelectric Sensors for Studying the Interactions with Nanoparticles

October 23, 2023

Tanaz Islam,[†] Olga N. Chesnokov,[‡] Andrew V. Oleinikov,[‡] and Peng Yi[†,*]

[†]*Department of Civil, Environmental and Geomatics Engineering, College of Engineering & Computer Science, Florida Atlantic University, Boca Raton, Florida 33431-6496, USA*

[‡]*Department of Biomedical Science, Charles E. Schmidt College of Medicine, Florida Atlantic University, Boca Raton, Florida 33431-6496, USA*

* Corresponding author: Peng Yi, Email: pengyi0124@outlook.com

Additional Information on Materials and Methods

Determining Aggregation Attachment Efficiency of HemNPs using Time-Resolved Dynamic Light Scattering (DLS). The Zetasizer (Nano ZS90, Malvern Instruments, UK) is equipped with a He-Ne laser with a wavelength of 633 nm and a DLS system which was used to determine the hydrodynamic diameter and the aggregation kinetics of nanoparticles. The DLS system measures the diffusion coefficient of nanparticles which is converted to the hydrodynamic diameter using the Stokes-Einstein equation.[1] For each aggregation experiment of HemNPs, a predetermined amount of electrolyte stock solution was introduced into the centrifuge tube containing 8.8 mg/L HemNPs suspension at 10 µM HCl such that the total volume of the final suspension was 1 mL. Immediately after that, the tube was swirled gently by a hand for less than ca. 10 s. The suspension in the centrifuge tube was quickly transferred to a dust free polystyrene cuvette (Sarstedt AG & Co. KG, Germany) which was then inserted into the chamber of DLS system for measurements. The intensity-weighted hydrodynamic diameters of HemNPs were monitored over time periods of 20-120 min. The time between the introduction of electrolyte stock solution and the start of the first DLS measurement was ca. 60 s.

The aggregation attachment efficiency (α_A),[2] also known as the inverse stability ratio, $1/W$,[1, 3] during the initial stage of HemNP aggregation under Brownian motion can be attained from time-resolved DLS measurements using the following equations:[1-4]

$$k_{11} \propto \frac{1}{N_0}\left(\frac{dD_h(t)}{dt}\right)_{t\to 0} \tag{S1}$$

where k_{11} is the second-order aggregation rate constant of primary nanoparticles for doublet formation, N_0 is the initial primary particle concentration, and D_h (t) is the intensity-weighted hydrodynamic diameter at time t.

$$\alpha_A = \frac{k_{11}}{(k_{11})_{fast}} = \frac{\frac{1}{N_0}\left(\frac{dD_h(t)}{dt}\right)_{t\to 0}}{\frac{1}{N_0}\left(\frac{dD_h(t)}{dt}\right)_{t\to 0,fast}} \tag{S2}$$

The term "fast" refers to the fast diffusion-limited or favorable aggregation at high concentrations of inert electrolytes. A linear least squares regression of the increase in $D_h(t)$ with t was used to obtain the initial rates of increase of $D_h(t)$. The $(dD_h(t)/dt)_{t\to 0}$ in favorable (or diffusion-limited) regime was determined using the initial 15 min of aggregation at 100, 300, and 500 mM NaCl, during which the $D_h(t)$ became 1.3 to 2.0 times the initial hydrodynamic diameter, $D_h(0)$. At 1

mM NaCl, the aggregation continued for 20–120 min since $D_h(t)$ increased much slower than the favorable regime, to 1.0–1.2 times $D_h(0)$ at the end.

Preparation for QCM-D Experiments. Before QCM-D experiments, the flow module was cleaned by a thorough rinsing with 2% Hellmanex III (Z805939, Sigma-Aldrich, MO), a surfactant solution, for 30 min and DI water for another 30 min at a flow rate of 0.6 mL/min. Then, the flow module was dried with ultrapure nitrogen gas (NI UHP300, Airgas, PA). The silica-coated sensors were soaked in 2% Hellmanex III for 30 min. Then, they were cleaned by thoroughly rinsing the sensor surface with ample amount of 2% Hellmanex and DI water, consecutively, followed by drying with ultrapure nitrogen gas, and oxidization in a UV-ozone chamber (Procleaner 110, BioForce Nanosciences, Inc., Ames, IA) for 20 min to remove organic impurities from the surface.

All the solutions were degassed by ultrasonication (Branson M3800, output power 115 W, frequency 40 kHz) for 10 min before introducing to the flow chamber. The temperature of the solutions was maintained at 27 °C in a water bath, 2 °C above the experimental temperature to avoid the formation of gas bubbles and temperature related artifacts.

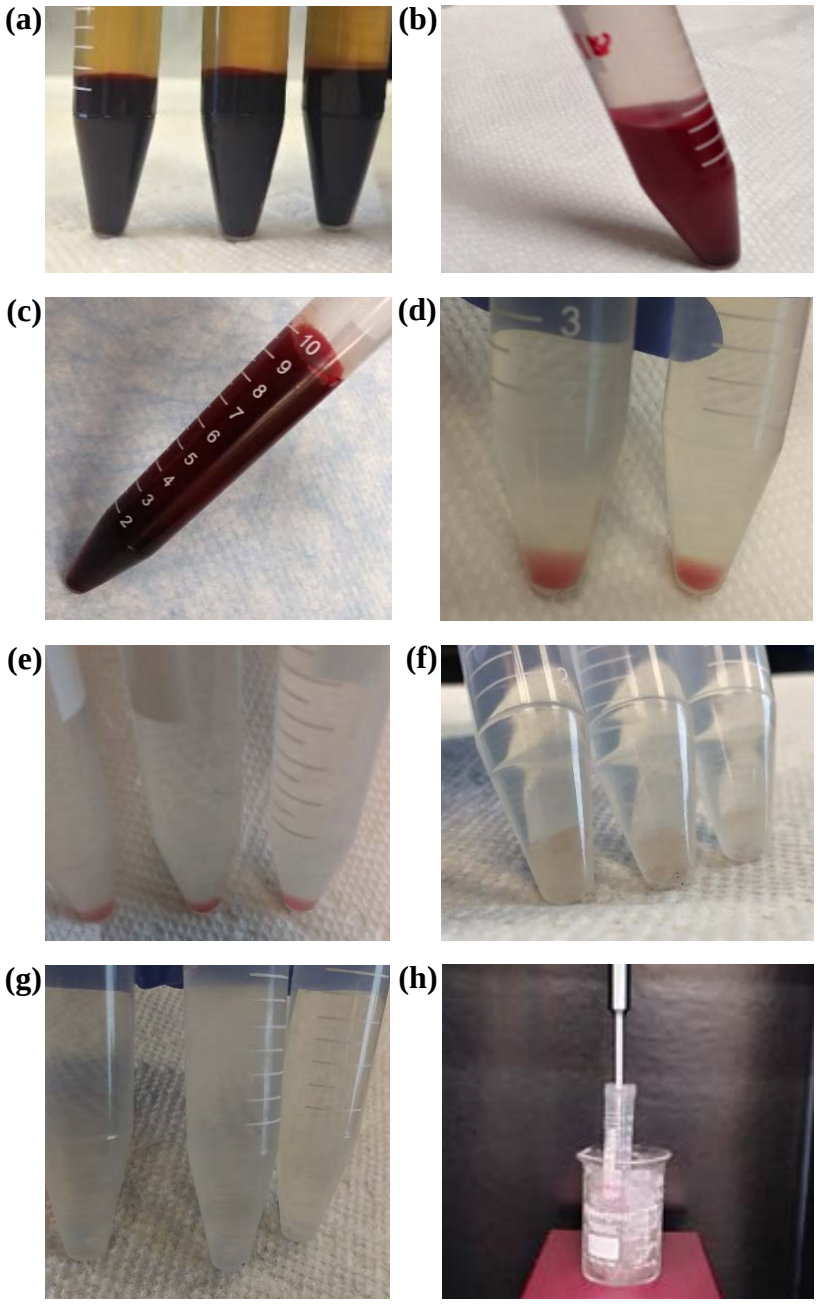

Figure S1. Photographs at each step of the preparation of RBCm suspension: (a) Isolation of erythrocytes from whole blood via centrifugation; (b) washed erythrocytes in PBS; (c) hemolysis of erythrocytes after the hypotonic treatment using 0.25×PBS solution; (d) the pink RBC ghosts after the final wash with 0.25×PBS; (e) the RBC ghosts after the first time wash with deionized (DI) water ; (f) whitish RBC ghosts after the final wash with DI water; (g) dispersed RBCm after keeping the whitish RBC ghosts in DI water at 3 °C in a refrigerator for three days; (h) sonication

of RBC membrane suspension in 1 mM NaCl and 0.2 mM $NaHCO_3$ using a probe sonicator in ice bath.

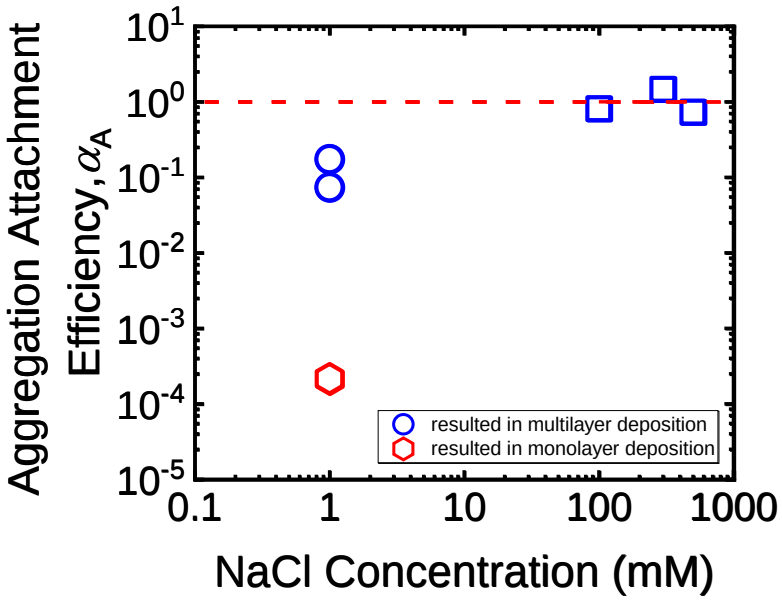

Figure S2. Aggregation attachment efficiencies of HemNPs as a function of NaCl concentration at pH 5.1.

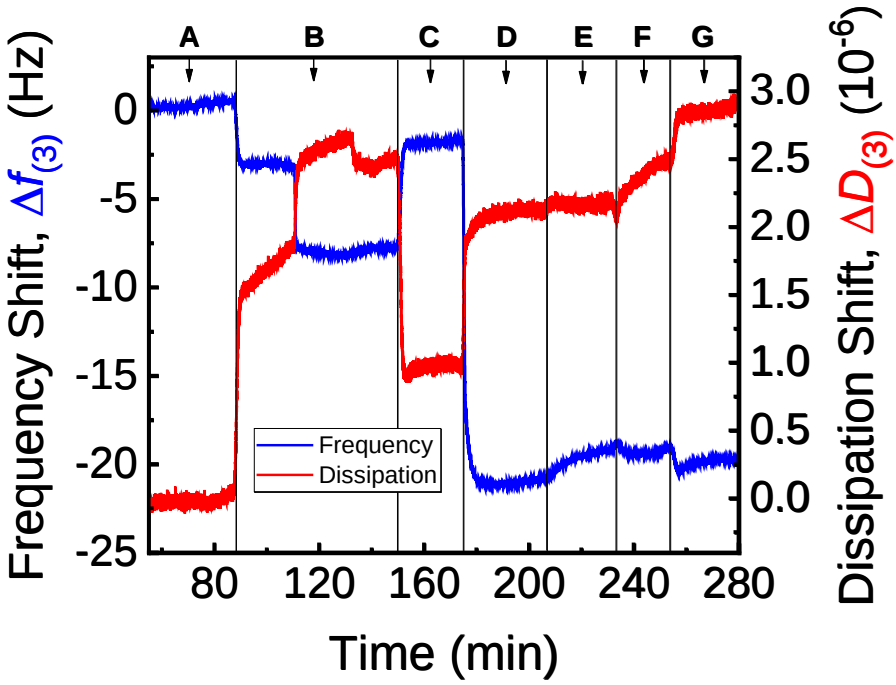

Figure S3. Complete profiles of frequency and dissipation of a QCM-D deposition experiment of 8.8 mg/L HemNPs (α_A = 0.0002) on SRBCm at 1 mM NaCl (pH 5.1), as a duplicate experiment for 'Figure 6a'. The stages are denoted by A to G. **A:** Rinsing silica surface with DI water; **B:** Formation of PLL coating on the silica surface; **C:** Rinsing PLL layer with 1 mM NaCl and 0.2 mM $NaHCO_3$; **D:** Formation of SRBCm at 1 mM NaCl and 0.2 mM $NaHCO_3$; **E:** Rinsing SRBCm with 1 mM NaCl and 0.2 mM $NaHCO_3$; **F:** Rinsing SRBCm with 1 mM NaCl (pH 5.1); **G:** 8.8 mg/L HemNPs at 1 mM NaCl (pH 5.1) was introduced, and the deposition of HemNPs on SRBCm occurred.

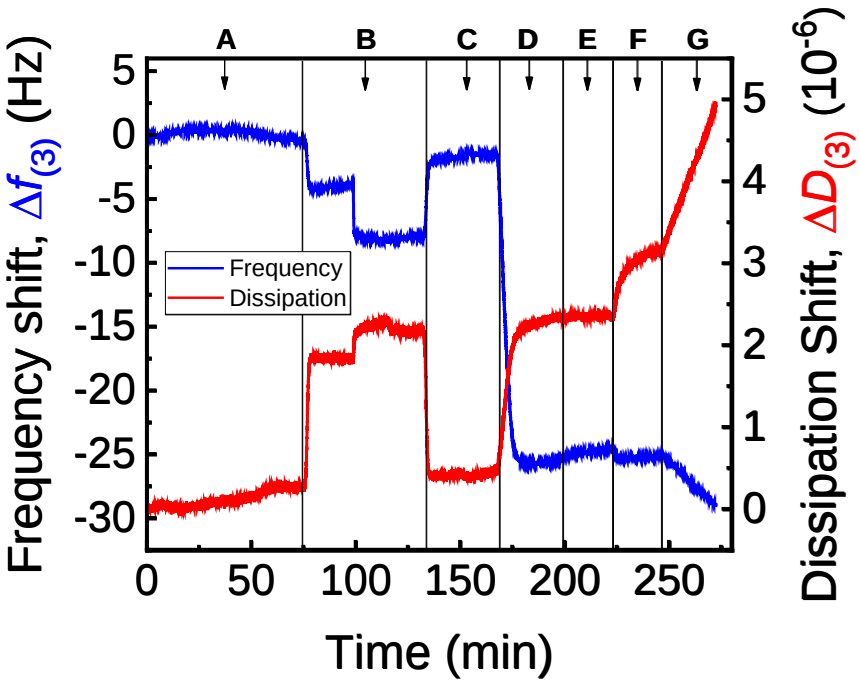

Figure S4. A complete frequency and dissipation profile during a QCM-D deposition experiment of 8.8 mg/L HemNPs (α_A = 0.173) on SRBCm at 1 mM NaCl (pH 5.1) which is a duplicate experiment for 'Figure 6b'. The stages of the QCM-D experiment are denoted by A to G. **A:** Rinsing silica surface with DI water; **B:** Formation of PLL coating on the silica surface; **C:** Rinsing PLL layer with 1 mM NaCl and 0.2 mM $NaHCO_3$; **D:** Formation of SRBCm at 1 mM NaCl and 0.2 mM $NaHCO_3$; **E:** Rinsing SRBCm with 1 mM NaCl and 0.2 mM $NaHCO_3$; **F:** Rinsing SRBCm with 1 mM NaCl (pH 5.1); **G:** 8.8 mg/L HemNPs at 1 mM NaCl (pH 5.1) was introduced, and continuous deposition of HemNPs on SRBCm occurred. Figure 2 presents Stage A, B, C, and D for the demonstration of SRBCm formation.

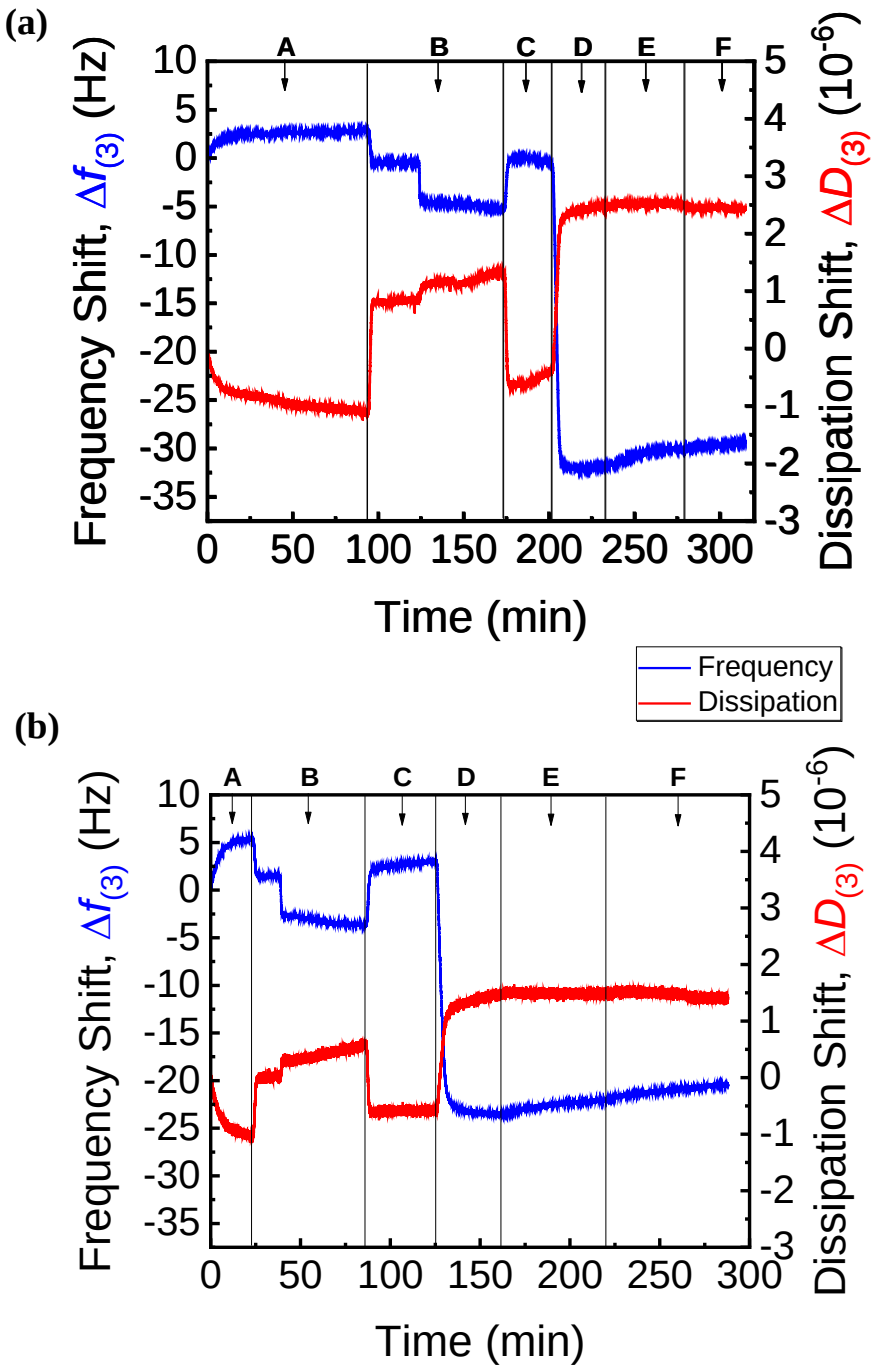

Figure S5. The entire frequency and dissipation profiles of QCM-D deposition experiments of 5 mg/L PSNPs on SRBCm at 1 mM NaCl and 0.2 mM $NaHCO_3$ (pH 7.0), for (a) the experiment shown in 'Figure 3a' and (b) another duplicate experiment. The stages are denoted by A to F. **A:** Rinsing silica surface with DI water; **B:** Formation of PLL coating on the silica surface; **C:** Rinsing PLL layers with 1 mM NaCl and 0.2 mM $NaHCO_3$; **D:** Formation of SRBCm at 1 mM NaCl and

0.2 mM $NaHCO_3$; **E:** Rinsing SRBCm with 1 mM NaCl and 0.2 mM $NaHCO_3$; **F:** 5 mg/L PSNPs at 1 mM NaCl and 0.2 mM $NaHCO_3$ was introduced and no deposition took place.

References

1. Holthoff, H.; Egelhaaf, S. U.; Borkovec, M.; Schurtenberger, P.; Sticher, H., Coagulation rate measurements of colloidal particles by simultaneous static and dynamic light scattering. *Langmuir* **1996,** *12*, (23), 5541-5549.
2. Chen, K. L.; Mylon, S. E.; Elimelech, M., Aggregation kinetics of alginate-coated hematite nanoparticles in monovalent and divalent electrolytes. *Environ Sci Technol* **2006,** *40*, (5), 1516-1523.
3. Kleimann, J.; Gehin-Delval, C.; Auweter, H.; Borkovec, M., Super-Stoichiometric Charge Neutralization in Particle−Polyelectrolyte Systems. *Langmuir* **2005,** *21*, (8), 3688-3698.
4. Yi, P.; Chen, K. L., Influence of Surface Oxidation on the Aggregation and Deposition Kinetics of Multiwalled Carbon Nanotubes in Monovalent and Divalent Electrolytes. *Langmuir* **2011,** *27*, (7), 3588-3599.